140-7
6

The Role of Residual Stresses in Ceramic Substrate Materials for Hybrid Thick Film Applications

by

Noel N. Schulz

Thesis submitted to the faculty of the
Virginia Polytechnic Institute and State University
in partial fulfillment of the requirements for the degree of

MASTER OF SCIENCE

in

Electrical Engineering

©Noel N. Schulz and VPI & SU 1990

APPROVED:

A. Elshabini-Riad, Co-chairman

Robert W. Hendricks, Co-chairman

Sedki Riad

February, 1990

Blacksburg, Virginia

c.2

LD
5655
V855
1990
S384

c.2

The Role of Residual Stresses in Ceramic Substrate Materials for Hybrid Thick Film Applications

by

Noel N. Schulz

Committee Co-chairmen:
A. Elshabini-Riad
Electrical Engineering Department

and

Robert W. Hendricks
Materials Engineering Department

(ABSTRACT)

This work presents introductory research to provide the relationship between electrical measurements and residual stresses caused by hybrid processing. X-ray diffraction is used to measure residual stresses in the ceramic substrate as well as metallization of wideband coplanar thick film probes. The probes are also tested for electrical performance using Time Domain Reflectometry (TDR) technique. This thesis presents results that indicate that significant tensile residual stresses were generated on the back of the substrate, particularly during the laser scribing phase of the finished device. Significant tensile stresses were also observed in the Silver-Palladium (Ag-Pd) metallization. TDR measurements indicated significant response variations which were attributed to these induced stresses. Attempts were also made to reduce these stresses by an annealing process in order to improve the TDR response uniformity.

ACKNOWLEDGEMENTS

The author wishes to express her sincerest gratitude to Dr. Aicha Elshabini-Riad and Dr. Robert W. Hendricks for their guidance, time, and invaluable support throughout this work. She also wishes to express her sincere thanks to the Riad and Hendricks families that have sacrificed time in the evenings and on weekends for this work.

Sincere thanks are also due to Dr. Sedki Riad for his support of time domain measurements and assistance as a committee member.

The author would like to thank the International Society of Hybrid Microelectronics and the Institute for Materials Science and Engineering of the Virginia Center for Innovative Technology for their financial support of this research. This support made it possible for the author to experiment in a new area at VPI&SU.

The author would like to thank Jinmyun Jo, Michel Laurent, Derome Dunn, Venki Iyer, and Nancy Morgan for their many discussions on interpreting the residual stress data.

The author expresses her gratitude to Kemal Fidanboylu, Narayanamoorthy Muthukrishnan, Ryp Walters, and Gus DiPierro for their help with thick film processing and time domain measurements.

In addition, special thanks are due to Monty Hayes and Karen Snider for their help and support throughout this work.

The author would like to express her heartfelt gratitude and love to her parents Butch and Joan Nunnally for all their love and moral support. Without their encouragement over the years, fewer dreams would have become realities.

Finally the author would like to thank her husband, Kirk Schulz, for his endless patience, support, and love especially in those times when the many deadlines seemed impossible.

Contents

Abstract ii

Acknowledgements iii

1 INTRODUCTION 1

2 STRESSES AND MICROELECTRONICS 3

2.1 Introduction 3

2.2 Existence and Nature of Stresses in Hybrid Thick Film Circuits 4

2.2.1 Thick Film Metallizations 4

2.2.2 Thick Film Resistors 5

2.3 Stresses and Simple Hybrid Thick Film Applications 10

2.4 Summary 14

3 RESIDUAL STRESSES 15

3.1 Introduction 15

3.2 Residual Stress Measurements Using X-ray Diffraction 16

3.2.1 Concept of the Technique 16

3.2.2 Previous Residual Stresses Work in Ceramics 23

3.3 Residual Stress Measurements on Thick Film Circuits 24

3.4 Summary 25

4 TIME DOMAIN REFLECTOMETRY 26

4.1 Introduction 26

4.2 Description of Time Domain Reflectometry 27

4.2.1 Concept of The Time Domain Reflectometry Technique 27

4.2.2 Previous TDR Research Conducted on Coplanar Probes 29

4.3 Measuring Electrical Properties of Coplanar Probes 31

4.3.1 TDR Measurements on Coplanar Probes 31

4.3.2 Modeling of Time Domain Reflectometry Measurements 31

4.4 Summary 33

5 MATERIALS AND PROCEDURES 35

5.1 Introduction 35

5.2 Materials, and Manufacturing and Processing Procedures 36

5.3 Procedures for Residual Stresses Measurements 37

5.3.1 Alumina Substrates 37

5.3.2 Silver-Palladium (Ag-Pd) Metallization 43

5.4 Measuring Electrical Properties of Coplanar Probes 45

5.4.1 Measuring TDR Responses of a Coplanar Probe 45

5.4.2 Modeling of TDR Responses 49

5.5 Correlation of Materials Processing with Residual Stresses and Electrical Measurements 49

5.6 Summary 51

6 RESULTS AND DISCUSSION 55

6.1 Introduction 55

6.2 Residual Stresses in the Ceramic Substrate 55

6.2.1 Characterization of Bare Substrates 55

6.2.2 Characterization of Processing Steps 57

6.2.3 Characterization of Annealing Steps 60

6.3 Residual Stresses in the Metallization 65

6.4 Time Domain Reflectometry Measurements 68

6.5 Summary 70

7 CONCLUSIONS AND SUGGESTED FUTURE WORK **71**

A Calculations **74**

A.1 Calculation of Stresses 74

A.2 Calculation of Diffracted Planes in Ag-Pd 76

Bibliography **77**

Vita **82**

List of Figures

2.1 Example of Multilayer Structure 6

2.2 Thick Film Strain Gauge 11

2.3 Thick Film Wideband Probe 13

3.1 Relationship of Stress on Crystalline Material 18

3.2 X-ray Diffraction of Crystalline Materials 19

3.3 Definition of Angles ϕ and ψ 20

3.4 Examples of d-spacing versus $\sin^2\psi$ plot 22

4.1 Diagram of Incident and Reflected Wave 28

4.2 Setup of TDR Work Station 28

4.3 Network model of the probe 30

4.4 Model Circuit Components and Respective Values 30

4.5 TDR Measurements on Probe 32

5.1 TEC Portable Apparatus for Residual Stresses 38

5.2 Alumina Diffraction Pattern 40

5.3 D versus $\sin^2\psi$ plot for Alumina 42

5.4 Silver-Palladium (222) Diffraction Peak 44

5.5 D versus $\sin^2\psi$ plot for Ag-Pd Metallization 46

5.6 Drawing of TDR Setup with Probe 48

5.7 TDR Measurements on Probe 50

5.8 Stress Measurements on Substrate 52

5.9 Processing Steps of Substrate 52

5.10 Stress Measurements on Metallization 54

6.1 Comparison of Normal and Shear Stresses for Processing 59

6.2 Weibull Distribution for Alumina 61

6.3 Comparison of Stresses for Low Temperature Anneal 63

6.4 Comparison of Stresses for High Temperature Anneal 64

6.5 Linear Regression of Low Temperature Anneal Stresses 64

6.6 Stresses in Circuit Due to TCE Mismatch 67

6.7 Comparison of TDR Open Circuit Measurements 69

List of Tables

5.1 Properties of Alumina Substrate 42

5.2 X-ray Constants for (146) Planes of Alumina 44

5.3 Compliance Matrices of Materials 46

5.4 Elastic Constants for Metallization materials 47

6.1 Normal and Shear Stresses in Bare Substrates 58

6.2 Normal and Shear Stresses as Probe 1A is processed 58

6.3 Normal and Shear Stresses for Different Anneals 63

6.4 Normal Stresses in Ag-Pd Metallization 67

Chapter 1

INTRODUCTION

As microelectronic substrate sizes increase with the simultaneous increase in circuit density and complexity, mechanical and thermal residual stresses both in the substrate as well as in the deposited films present an increasing problem, especially in multilayer structures. In addition, in several phases of the production of these circuits, such as electrical testing and packaging, and in many environmental applications, external stresses may be placed on the structure. These external stresses, combined with any residual stresses, have been observed to induce failures ranging from cracking and warping of the ceramic substrates and loss of continuity of the metallizations to breakdown of the various dielectric, resistive, or magnetic layers and the delamination between the film components and the substrate. In addition, electrical properties are degraded due to the induced stresses even when mechanical failure is not clearly observed. The degradation due to the induced stresses includes phase distortion, loss of continuity, and attenuation. Therefore, it is important to observe the presence of residual stresses and to understand the cause of their existence in the substrate.

This work addresses the role of stresses in hybrid thick film applications. These stresses become apparent when manufactured hybrid circuits fracture during testing. This research set out to understand how various processing steps of a thick film coplanar, wideband probe affect stresses in the ceramic substrate and metallization and how these stresses affect the

electrical performance.

This thesis outlines this investigation of the role of residual stresses in ceramic substrate and metallization materials used in hybrid thick film applications. Chapter 1 is a general introduction. Chapter 2 presents a literature survey on various stresses associated with thick film devices. The electrical and physical characteristics of the coplanar probe are also discussed.

Chapter 3 presents general information about residual stress measurements. In this chapter, the use of x-ray diffraction (XRD) techniques to determine residual stresses in materials, particularly ceramics and metallization, are discussed. Also contained in this chapter is a description of the general technique used in XRD stress measurements.

In Chapter 4, the electrical measurement technique, Time Domain Reflectometry, is discussed. The first part of the chapter presents the method for characterizing devices at high frequency. The second part discusses the general technique used in TDR measurements.

Chapter 5 presents the materials and experimental procedures used in the thesis research. First, the materials used are discussed. Next, the thick film fabrication process of the probe is presented. Following this, the specifics of the TDR and XRD measurements are outlined.

Chapter 6 outlines the results obtained using the experimental procedures indicated in Chapter 5. The explanation and discussion of the implications of these results are presented in this chapter.

Finally, Chapter 7 summarizes the work conducted in this research and provides a brief description of future work related to the correlation of residual stresses and the electrical performance of devices.

Chapter 2

STRESSES AND MICROELECTRONICS

2.1 Introduction

Recently, stresses in microelectronics have become a crucial issue as designers attempt to achieve better performance of proven materials. Understanding and modeling the electrical changes caused by stresses help engineers in the design area to accurately determine the performance of hybrid circuits. In addition, by obtaining a more in-depth understanding of the mechanical failures caused by stresses, new procedures can be devised to eliminate or reduce these stresses.

This chapter highlights the published work by previous investigators relating stresses and thick film circuits. The chapter also contains a section detailing the thick film coplanar wideband probe.

2.2 Existence and Nature of Stresses in Hybrid Thick Film Circuits

The mismatch of the thermal expansion coefficient of materials can cause mechanical stresses in electronic assemblies when the environmental temperature changes. Large stresses may develop during high temperatures experienced in the fabrication, shipping and storage stages [1]. In addition, the temperature cycling that occurs in normal operations may induce cyclic stresses that lead to fatigue-type failures [1]. The thermal problem has become even more evident recently as high-density packaging and power requirements have made operating conditions even more severe [2]. In addition to internal stresses, testing and operation may require that external stresses are applied to the circuit. Such stress problems have been encountered over the years in the electronics industry whether it relates to printed circuits boards, thick film circuits, or integrated circuits.

This section outlines the work done to associate electrical properties with stresses, both internal as well as applied. This section also highlights the work achieved on thick film conductors and resistors elements.

2.2.1 Thick Film Metallizations

Little work has been done to investigate the role of stresses in conductors. Riemer [3] outlines work done to investigate substrate warpage or breakage due to the stresses caused by the conductor paste. In his work, he determined that the warpage was caused by non-uniform heat radiation from the substrate during the cool-down phase. Because substrates move quickly through the furnace, most of the heat is transferred by radiation. However, different materials emit and absorb radiation at different rates. As substrates with thick film paste move through the furnace, the radiation characteristics of that paste change.

During the firing process, both the substrate as well as the paste are relatively good absorbers of the heat. When the substrate moves into the cooling zone after the firing

process, the mean wavelength of the radiation is longer. Dielectric and substrate materials do not change properties so they easily emit the heat absorbed at firing. However, the conductor paste changes radiation characteristics once it is fired as metallization. The fired metallization can hardly emit heat, trapping previous absorbed heat in the metallization. This fact means substrates cool rapidly where there is no conductor paste and do not lose much heat where conductor paste is deposited. This effect causes heat to be trapped under the metallization and results in an uneven temperature distribution. The temperature gradient and mismatch of the thermal expansion constants between the fired paste and the substrate produce substantial stresses. Depending on the magnitude of these stresses, the substrate may warp or even fracture.

2.2.2 Thick Film Resistors

While limited work has been done with metallizations in the thick film technology, much research has concentrated on the stress sensitivity of thick-film resistor elements. This research involves two areas, namely: (1) residual stresses caused by processing, assembly, and packaging, and (2) externally applied stresses.

Research in the area of stresses caused by processing, assembly, and packaging focuses mainly on the mismatch between thermal coefficients of expansion between the various materials. Completed hybrid circuits incorporate a wide range of materials ranging from oxides for substrates, metals for conductor runs, and plastics for coatings. Figure 2.1 illustrates a group of materials used to manufacture a device with variation in the linear thermal coefficients of expansion (TCE).

Stresses may be linked to processing such as laser trimming of thick film resistors. Shah and Berrin [4] used observations from Scanning Electron Microscopy (SEM) and the theory of drift mechanics to offer insight into the mechanism of the post-trim drift of the laser-trimmed thick film resistors they studied. They found two components of the drift: an instantaneous short term drift and long term drift. The short term drift was thickness dependent and caused by a gradient of compressive and tensile stresses in the fired film on

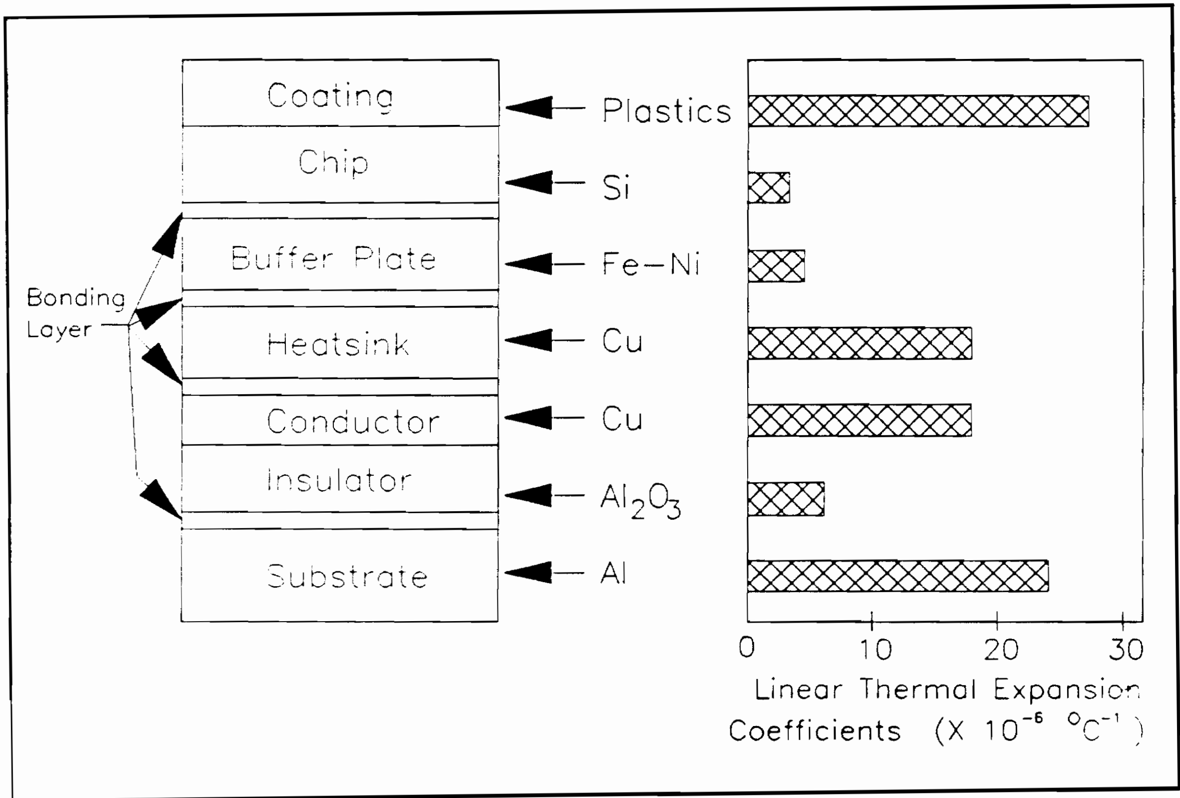

Figure 2.1: Example of Multilayer Structure in Hybrid Technology [2]

a rigid substrate. They attributed these stresses to the TCE mismatch and/or quenching stresses produced during the firing process. The tensile stresses in the film increased upon an increase of the film thickness and consequently reduced the crack resistance of the film. Therefore, cracks could form and propagate more easily in thick resistors rather than thin resistors. The investigators also found that applying a protective overglaze coating reduced the drift in values considerably. The reason was attributed to the fact that the slight mismatch of the coating would place the resistor film in compression, thus reducing the post-trim drift and would also increase the crack resistance of the film.

Stress problems have also been identified in the areas of assembly and packaging. Riemer and Russell [5] reported an analysis of stresses in the solder fillets of conventional chip carriers on ceramic substrates. They found cracks in these solder fillets. These failures occurred during temperature cycling without the power applied. The cracking of the solder fillets of chip carriers was explained by the thermal stresses between the solder and the ceramic at temperatures as low as -65°C. Because of the difference in thermal coefficients of expansion between the two materials, tensile stresses develop in the solder which are relieved through the cracks. The researchers proposed an alternative technique to sandwich the solder between the chip carrier and the ceramic in order to reduce these tensile stresses.

In another stress problem associated with assembly and packaging, Reshey [6] reported failures of the epoxy used to seal a ceramic lid to a substrate. The epoxy was applied directly on the thick film elements so the lid could be attached. The thermal coefficient of expansion (TCE) mismatch between the epoxy and alumina lead to cracks in resistors and the delamination of conductor traces during thermal cycling. The cracks caused changes in resistance while the delamination pulled the conductor off the substrate causing breaks in the continuity of the circuit. However these problems were eliminated by printing a flexible buffer layer between the resistor and the lid sealant. The buffer layer had a TCE approximately midway between the ceramic and epoxy and thereby reduced the thermal stress by a factor of ten.

Besides the investigation of the internal interactions of materials in hybrid circuits, more

work has been done on the effect of applied stresses to thick film resistors. Published work in the literature [7 – 12] covers the investigation of the strain sensitivity of thick film resistors, a phenomenon also called the piezoresistive effect.

Holmes [7] was one of the first to report changes in resistance values due to substrate flexure. His experiments involved bending the substrate so the resistor was first in compression and then in tension. He found that changes in resistance values were linear, reversible, and reproducible with no hysteresis. The lack of hysteresis indicated that the changes resulted from elastic distortion rather than permanent damage. In the two resistor pastes Holmes used, Dupont Birox 1021 and 1051, the resistance value increased with the resistor in tension and decreased with the resistor in compression. These trends were confirmed in references [8 – 11]. Canali [9] also showed that strain sensitivity increases with increasing sheet resistance. These results indicate that the transport mechanism plays a dominant role in the piezoresistive properties with respect to the geometrical change induced by strain [9,10].

Another interesting point is the effect of the same magnitude of stresses applied normal or parallel to the current direction. Canali, Malavasi, Morten, Prudenziati, and Taroni [10] reported that the curve of stress versus resistance has a different slope measured in the two different directions. The longitudinal strain line had a larger slope and corresponding gauge factor. The gauge factor represents the relative change (ΔR/R) of the resistance induced by the strain (ϵ) as illustrated in the equation,

$$GF = \frac{\Delta R}{R\epsilon} \tag{2.1}$$

The experimental relationship between the gauge factors in the longitudinal and transverse directions agreed well with an equation given in [8]

$$GF_{LM} - GF_{TM} = 2(1 + \nu) \tag{2.2}$$

where ν is Poisson's ratio of the substrate and GF_{LM} and GF_{TM} are the gauge factors in the longitudinal and transverse directions, respectively. This equation holds for materials

that behave as isotropic materials. Therefore, the correspondence of thick film resistors suggests that they behave as isotropic materials.

It also follows from elasticity theory that the two gauge factors are different and the materials are isotropic. When the material is strained in one direction, the other direction is strained with the opposite sign as required by elasticity. These compensations alter the length and width values of the resistor and in turn its resistance. However, compensations in the longitudinal and transverse directions cause the same magnitude of change but have different effects on the resistance value.

Shah [11] varied the processing steps to observe the effect on strain sensitivity. He tested laser trimmed, untrimmed, overglazed, as well as not overglazed resistors. He also investigated the role of thickness on strain sensitivity. His results showed that untrimmed resistors showed the same characteristics reported by Holmes [7] independent of resistor geometry, thickness, or overglazing. However trimmed resistors were not as consistent. While trimmed resistors with thicknesses less than 0.5 mil had results similar to untrimmed resistors, resistors with thicknesses over 0.5 mils showed large, irreversible positive post-trim drifts up to ten percent of their original value. This effect was attributed to large tensile stresses caused by the TCE mismatch between the resistors and the substrates. SEM results showed that alumina (Al_2O_3) dissolved into the paste causing a concentration gradient of Al_2O_3 across the resistor thickness. This gradient acted as a buffer layer and had a TCE value between the two materials and helped reduce the tensile stresses in thin resistors but was not significant enough to help thick resistors.

Dell'Acqua et. al. [12] took a different approach to investigate the long term stability of thick film resistors. They used two techniques, an alumina diaphragm and a cantilever structure, to show that resistance drift is enhanced by an applied load. In tests lasting over 1000 hours resistors in compression tended to drift about forty percent less than those in tension.

Because of the piezoresistive characteristics demonstrated in references [7 – 12], thick film resistors have been targeted as good elements for strain gauges. The thick film strain

gauge has the ability to provide good performance at low cost, under a wide variety of environmental conditions [13]. While thin film gauges have been used in the past, several problems with this technology exist. Thin film technology requires high initial capital equipment costs, new tooling costs for different configurations, and precise process control demands [13]. Semiconductor resistors present another type of gauges that possess high gauge factors but show a large temperature coefficient of electrical properties. While thick films have lower gauge factors, they have small temperature coefficients of electrical properties [14].

The thick film strain gauge proposed in references [13 – 16] uses an alumina diaphragm on which four film resistors were connected in a Wheatstone bridge configuration. An example of this structure is shown in Figure 2.2. These sensors have many applications in automotive pressure sensing situations. One group of researchers proposed a system where the alumina diaphragm and a laser trimmed signal conditioning circuit are integrated on a common alumina substrate producing a useful complete gauge [16].

The main research findings have shown that thick film components are susceptible to stresses. While in the case of strain gauges, these characteristics are used as a measuring device, the internal stresses of the circuit caused by thermal stresses may lead to changes in the electrical characteristics and result in a decrease in reliability.

2.3 Stresses and Simple Hybrid Thick Film Applications

The basis for the present research lies in the determination of the relationship between stresses and a specific thick film device, a wideband or radio frequency (RF) probe. During testing, several probes shattered when external forces were applied to make test connection for impedance measurement. However, failures were not observed when probes that had been processed in a different manner were tested. Hence, the following work was undertaken to understand how the stresses induced by various processing steps caused mechanical failures and possibly electrical characteristic changes.

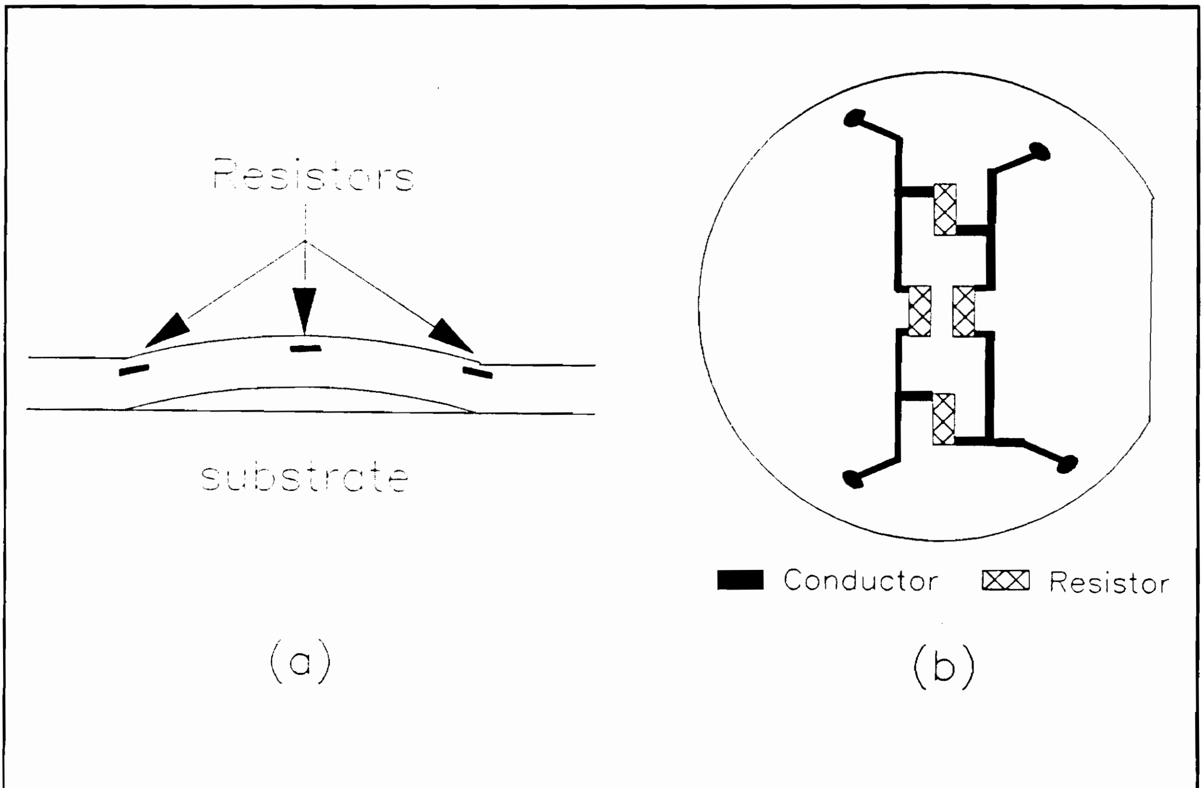

Figure 2.2: (a) Cross-section of alumina substrate and thick film diaphragm. (b) Layout of thick film strain gauge [16].

Before investigating the stress-electrical properties relationship of the probe, it is important to understand the device used to carry out these experiments. This section describes the physical and electrical properties of the wideband probe as well as illustrates the importance of the probe in high frequency testing. This discussion is based on reference [17]. The reference contains more detailed information on the probe.

The wideband coplanar probe possesses many features in common with coplanar waveguides. Both structures have a center conductor and split ground planes on both sides of the center conductor. The major difference between them is that, in the case of wideband coplanar probe, the ground planes are tapered down to the dimensions suitable for probing planar transmission lines. Figure 2.3 illustrates the layout of the probe and a photograph of the probe. The coplanar probe is designed to maintain a uniform characteristic impedance of 50 Ω along the length of the line. The probe is tapered to adapt to the planar line under test at one end and a coaxial to coplanar connector at the other end. Thus, coaxial to planar geometry is reasonably achieved.

The coplanar probe offers an alternative for testing high frequency components such as striplines, microstriplines, and coplanar waveguides. The coplanar probe has two advantages, namely: low parasitics or stray capacitance and inductance, and better calibration and reproducibility than other coaxial to planar adapters. A coaxial probe introduces parasitic fringing effects when used with planar geometries. These parasitic effects, typically inductive in nature, occur at the probe tips where the calibration reference plane is located. Because these parasitic signals alter the reference point for later measurements, serious unavoidable errors are incorporated into the data. On the other hand, with the coplanar probe, the transition from coaxial to planar geometry is located away from the reference plane and thus provides a better definition for the reference plane.

Probes, particularly coplanar probes, provide better calibration and reproducibility because they can be permanently soldered to a connector. This setup, which consists of the probe, the connector, and the cable, can be used on different components, to give a common frame of reference.

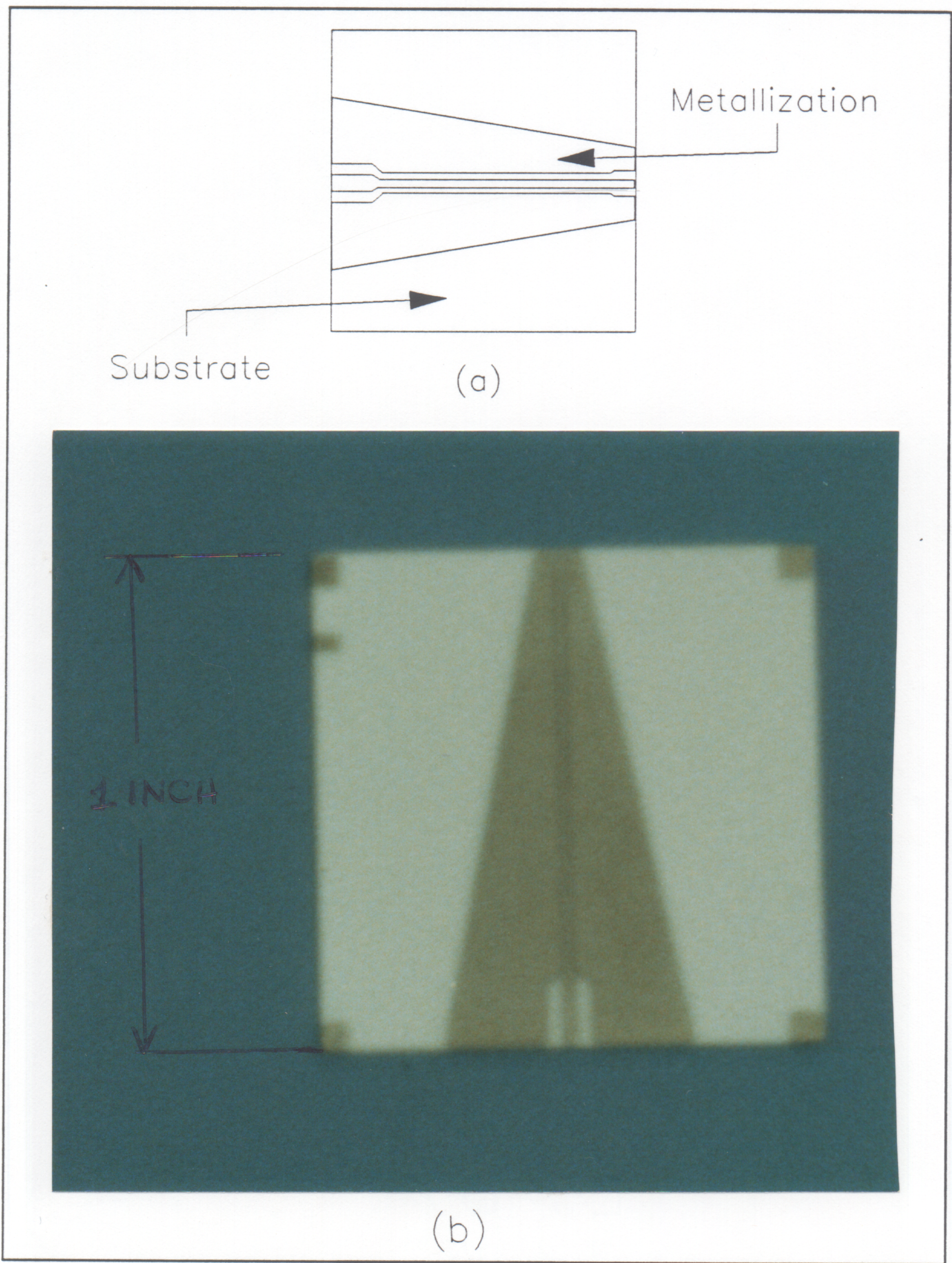

Figure 2.3: Thick Film Wideband Probe: (a) Layout (b) Photo

The coplanar probe was chosen for this research because of the simplicity of the circuit. On the other hand, the electrical equivalent model possesses a complex nature due to the tapering effect. The thick film system combines an alumina substrate and one type of thick film paste. By understanding some of the interactions of the conductor paste and the substrate, the goal is that the underlying principles investigated here can be extended to more complex circuits.

2.4 Summary

This chapter has illustrated that stresses have been investigated in various thick film applications. The work conducted in that respect has tried to determine models for understanding how stresses affect electrical values such as the resistance value. The details and importance of the thick film wideband probe have been also discussed.

Chapter 3

RESIDUAL STRESSES

3.1 Introduction

Mura [18] defines residual stresses as the "self equilibrating internal stresses existing in a free body which has no external forces or constraints acting on its boundary". In other words, residual stresses are stresses that remain after external loads are removed from the system. At the present time, residual stresses play a major role in the performance of materials. These stresses can arise during the various processing steps in engineering materials such as bending, forming, grinding, heat treatment, stress corrosion cracking and welding or as a result of phase transformations. If stress-inducing factors can be understood and properly controlled, then residual stresses can be used to enhance the properties of various materials or removed when their effects are deleterious [19].

Techniques to measure residual stresses are divided into two categories: destructive and non-destructive. One destructive technique combines the use of metal foil strain gauges with hole drilling. Gauges measure the released strain caused by drilling a hole. Using the measured values, back calculations can determine the value and gradient of the stresses in the material. The major disadvantage of this technique as well as other destructive techniques is once these holes are drilled the object under test is damaged [20]. Additionally,

hole drilling is difficult to use with brittle materials such as alumina as well as with very small parts.

Non-destructive techniques use other physical principles to measure residual stresses. Such techniques include magneto-acoustic, magneto-elastic, and ultrasonic techniques, and neutron and x-ray diffraction. As the names imply, these techniques are not destructive and the tested object is still functional. Although x-ray diffraction is an expensive technique, it has developed into a reliable, accurate, and fast technique for determining effectively residual stresses [20]. Besides offering a non-contact and nondestructive technique, x-ray diffraction allows the measurement of absolute stresses instead of only relative stress changes.

3.2 Residual Stress Measurements Using X-ray Diffraction

3.2.1 Concept of the Technique

The concept of the measurement technique using x-ray diffraction is covered in depth in the work presented by Noyan and Cohen [21]. This reference is offered as an excellent source for further details on the theory and practice of x-ray stress measurements.

X-ray diffraction is an accurate and reliable nondestructive method to determine residual stresses in crystalline materials. For a material with randomly oriented grains, the orientation of a given set of crystal planes relative to the residual stresses in the material varies from grain to grain. Therefore, if the material is sufficiently fine-grained, these crystal planes may be found at almost any orientation to the residual stresses in the material.

Figure 3.1 (a) shows a crystalline structure of a material without stress and with a lattice parameter d_o. If a force is applied to the material as shown in Figure 3.1 (b), elastic distortions of the crystal structure will become evident. Although the d-spacings change because of the stresses, the volume of the material must remain the same because of Poisson's effect and the incompressibility of the material. The elastic distortions depend on the orientation of the stresses relative to the atomic planes in the material, and appear

as a decrease in interplanar spacing (d-spacing) for crystal planes parallel to residual tensile stresses (d_1) and as an increase in d-spacing for crystal planes perpendicular to such stresses (d_2) as shown in Figure 3.1 (b). The difference between the interplanar spacing, Δd, for planes at different orientations can be used as internal strain gauges.

When an x-ray beam is incident on a material, it is diffracted by planes with a specific orientation to the beam as shown in Figure 3.2 (a) and produces a diffraction peak. A typical diffraction peak for alumina is shown in Figure 3.2 (b). The K_α splitting, seen in this figure, will be discussed later. The spacing of the planes and angular position of the diffracted x-rays are related to each other by Bragg's law. The equation takes the form

$$n(\lambda) = 2d\sin\theta \tag{3.1}$$

where λ is the wavelength of the radiation and 2θ is the angle between the incident and diffracted beam. If the specimen is tilted, diffraction occurs from the same planes in other grains. These grains are more nearly perpendicular to the stresses. These different grains produce other diffraction peaks slightly shifted from the previous one. From this shift in peak, $\Delta\theta$ can be determined and related to the change in d-spacing by differentiating Bragg's law:

$$\Delta d = -d\cot\theta\Delta\theta \tag{3.2}$$

Besides the change in θ, two other angles are related to the orientation of the stresses. Figure 3.3 shows these angles and the coordinate system used for making stress measurements. If σ_{33} is assumed to be zero and $\phi = 0$, the variation of d-spacing with ψ-tilt is related to the residual stresses by an equation of the form:

$$\frac{d_{0,\psi} - d_{0,0}}{d_0} = \frac{1+\nu}{E}\left[\sigma_{11}\sin^2\psi + \sigma_{13}\sin 2\psi\right] \tag{3.3}$$

where $d_{0,\psi}$ is the measured d-spacing of planes which forms an angle ψ with the material's

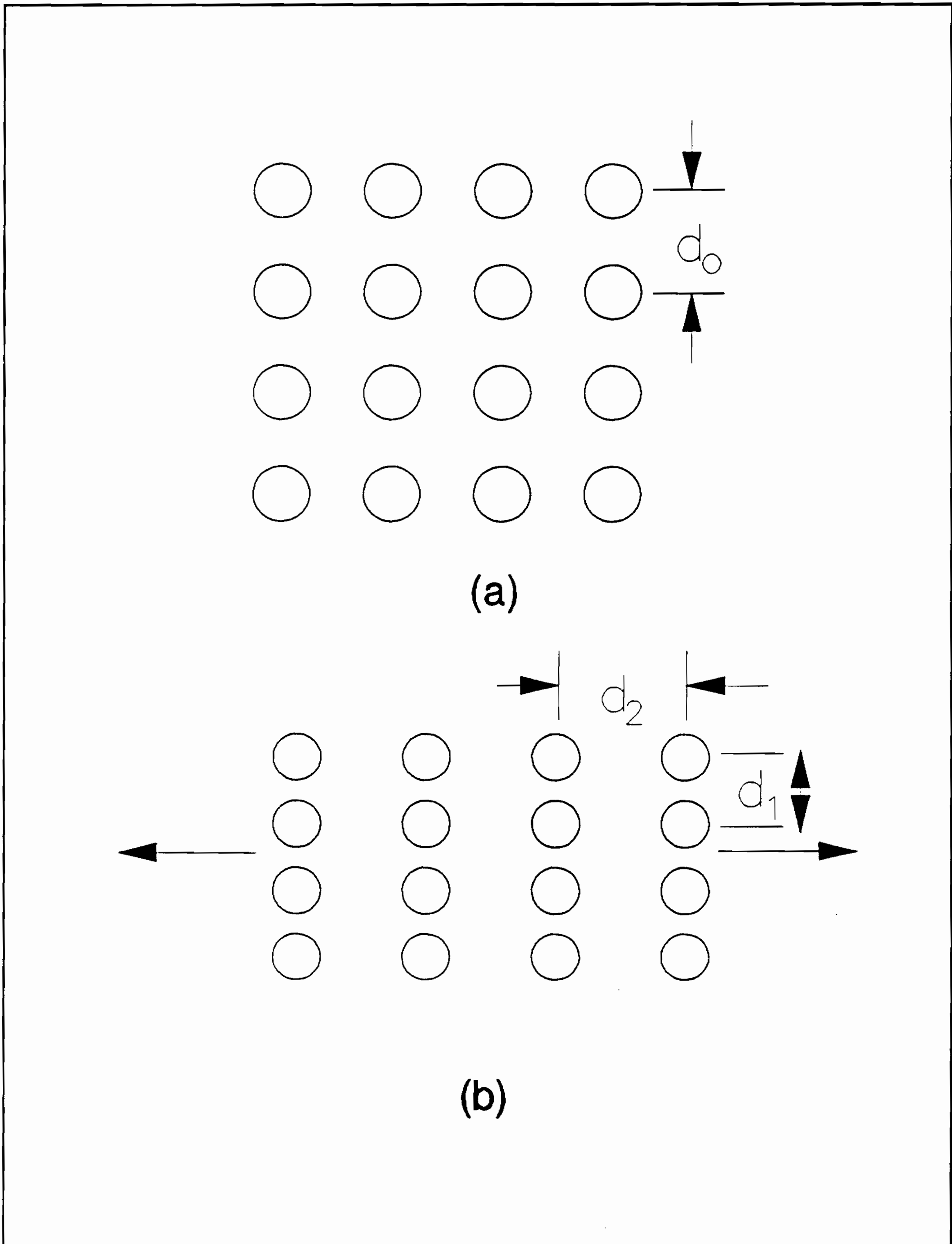

Figure 3.1: (a) Crystalline structure of material without stress. (b) Material with stress.

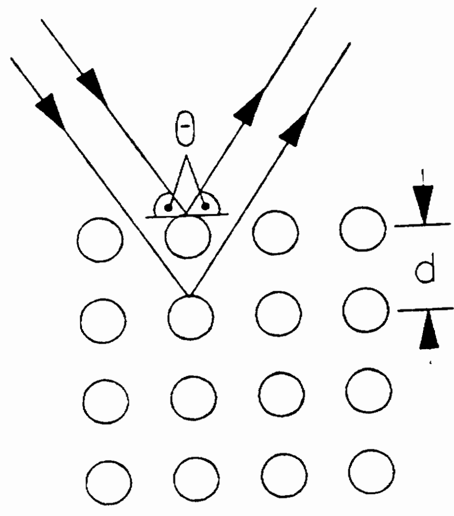

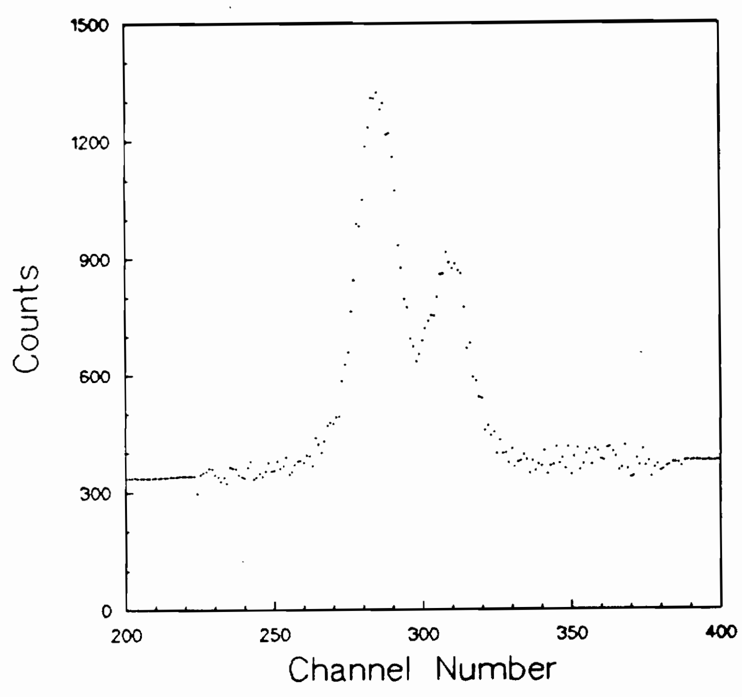

Figure 3.2: (a) X-ray beam diffracting off of crystalline material. (b) Diffraction peak of Alumina (146) planes.

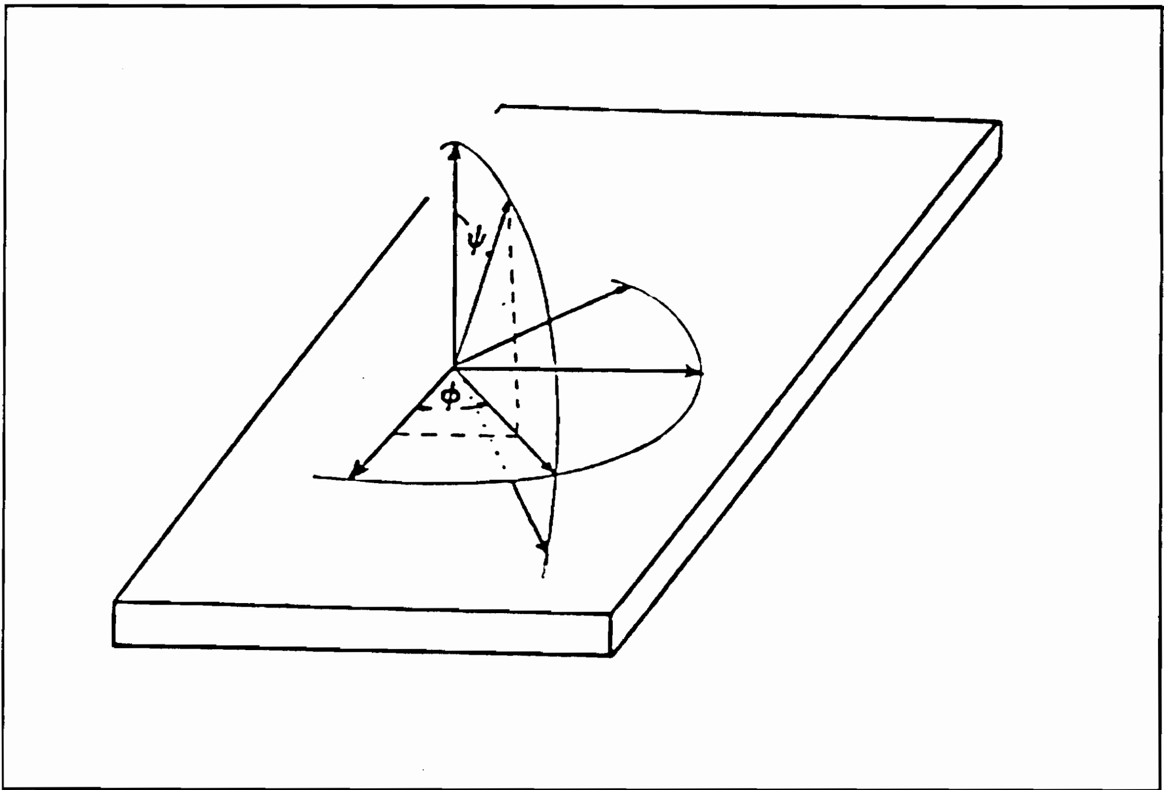

Figure 3.3: Definition of Angles ϕ and ψ [21].

surface in the $\phi = 0$ direction, $d_{0,0}$ is the d-spacing for $\psi = 0$, d_0 is the d-spacing of the unstressed planes, ν is Poisson's ratio for the material, E is the x-ray elastic constant, σ_{11} is the normal stress, and σ_{13} is the shear stress in the $\phi = 0$ direction. If the measurement is made at $\phi = 90^o$, the σ_{11} and σ_{13} terms in equation 3.3 become σ_{22} and σ_{23}, respectively. Equation 3.3 assumes that there are no stresses normal to the substrate surface (i.e. $\sigma_{33} = 0$). A set of five to ten measurements are taken using different ψ angles. The d-spacing and ψ angles are then related in a d versus $\sin^2\psi$ plot. If σ_{13} is set to zero, the plot of d versus $\sin^2\psi$ will yield a straight line with a slope proportional to the magnitude of the residual stresses in the ϕ-direction in the material. In performing the calculation of σ, the d-spacing for $\psi = 0$ is substituted for d_o since a completely stress-free reference sample is difficult to obtain and only a small error (less than 0.1%) is created by this substitution [21]. Shear stresses σ_{23} and σ_{13} can be obtained by a multiple regression of the d-spacings versus $\sin^2\psi$ and $\sin 2\psi$.

Figure 3.4 (a) shows a typical d versus $\sin^2\psi$ plot from Al_2O_3. The plot demonstrates a zero normal stress and small shear stresses. Deviations of the measurements from the fitted line are attributed to shear stresses. The presence of shear stress terms (σ_{13} and σ_{23}) implies that the main principle stresses are rotated with respect to the measurement coordinate system. Figure 3.4 (b) shows a d-versus $\sin^2\psi$ plot from the Ag-Pd metallization. The slope of the regression line shows a large tensile normal stress with no shear stresses. It is results such as these which comprise the bulk of our stress analysis as will be discussed in Chapters 5 and 6.

In order to determine the values of the residual stresses, the two constants, ν and $E(hkl)$ must be known independently. However, if we assume that σ_{33} is zero, then only the ratio $(1 + \nu)/E$ must be known. These constants are used to relate the internal strains (ϵ) to stress values as indicated by Hooke's Law. These elastic constants vary with different crystallographic orientations and with composition of the material. This variation has been shown by Tanaka et al. [22] and will be discussed later. If specific values for the constants of the polycrystalline material are unknown, it is possible to compute the x-ray modulus using single crystal elastic constants.

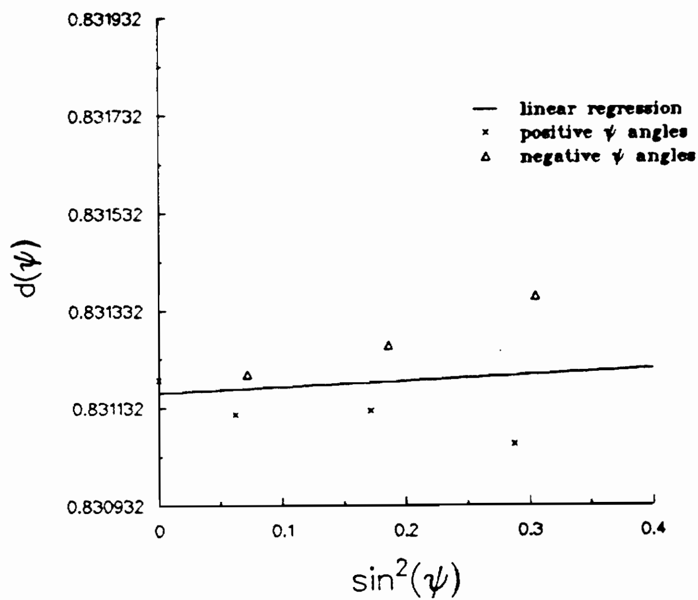

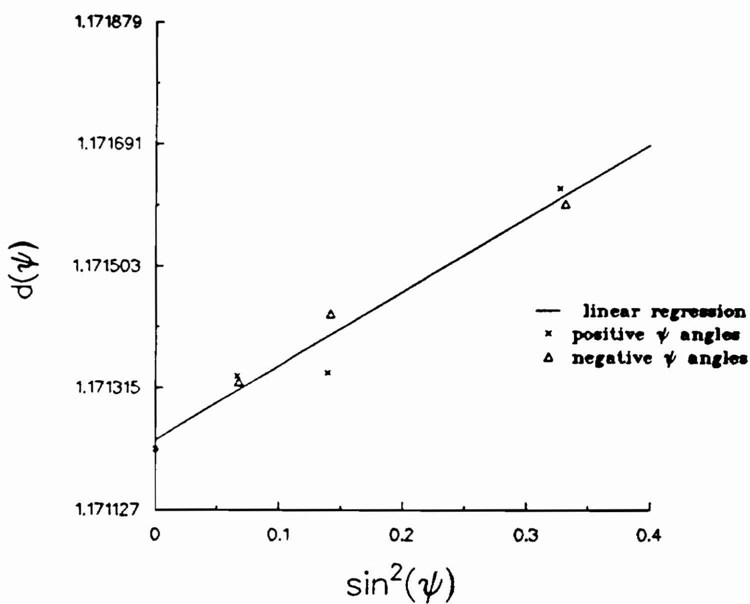

Figure 3.4: (a) d versus $\sin^2\psi$ plot for Alumina. (b) d versus $\sin^2\psi$ plot for Ag-Pd Metallization

Two important parameters of x-ray diffraction are the depth of measurement and the area of analysis. The depth of penetration of x-rays, and thus stress measurements, depends on the absorption coefficient of the material [21]. Typical depth values range from one to ten microns. The area of analysis for x-ray diffraction depends on the instrument. Areas as small as 0.1 mm^2 can be analyzed but more typical values, especially for portable systems, is 1 to 10 mm^2 [23].

3.2.2 Previous Residual Stresses Work in Ceramics

A wide range of residual stress experiments have been performed on ceramics, in particular alumina. Experiments have involved a variety of shapes of alumina including cylindrical bush [24], rods [25], bars [26,27], and armor tiles [28]. In addition, Gardner and Beauchamp [29] have investigated how laser machining affects the fracture strength of alumina.

While this research provides insight into the research of alumina substrates for thick film applications, two articles are of particular importance. Ruud and Gazzara [28] investigated alumina ceramic tiles for composite armor. Measurements were taken in four locations on a 5.6 x 5.7 x 0.5 inch (142 x 145 x 13 mm) alumina tile: at one corner, in the center, and along two edges. They revealed that the stress in the corner was 11 ksi (77 MPa) more compressive than in the center and the edges were 8 ksi (56 MPa) more compressive than in the center. These trends were attributed to air cooling from the high temperature annealing process used in the manufacturing of the tile.

A second paper of interest, by Gardner and Beauchamp [29], investigated the effects of laser machining on the fracture strength of 96% and 99.6% alumina substrate materials. Substrates (1.75 x 1.75 x 0.025 in (44.5 x 44.5 x 0.64 mm)) were laser scribed from a larger substrate size. Concentric circular holes, 0.1875 in (4.76 mm) in diameter, were cut in a group of substrates. Some samples were annealed while other remained untreated. Their results showed that the mean fracture strength of the 99.6% Al_2O_3 substrate with the holes was reduced by almost 50% compared to the corresponding unannealed blanks. This percentage decreased to 37% for annealed samples. However, no significant changes

in 96% alumina samples were observed regardless of whether the material was annealed, unannealed, laser machined, or blank.

These two experiments outlined two major areas of interest for the current research work on alumina substrates: the homogeneity of the ceramic substrates and the effect of processing, in particular laser machining, on the stresses developed in the substrate.

3.3 Residual Stress Measurements on Thick Film Circuits

The residual stresses were measured with a Technology for Energy Corporation Model 1610 portable apparatus for residual stress (PARS). This machine uses an omega geometry goniometer to collect data. A position-sensitive detector is rigidly mounted in the region of a high 2θ diffraction peak behind a low power x-ray tube. The tube-detector assembly is rotated above the sample to collect diffracted intensity at several ψ angles. An on-board computer calculates the d-spacing for the peak at each angle, using standard x-ray diffraction corrections for such effects as background, Lorentz polarization, and sample absorption. Then, it generates a plot of d versus $\sin^2\psi$ and calculates the residual stresses from a fitted straight line, based on the assumption that the stresses are biaxial.

The on-board computer does not have the capability to determine the shear stresses of a sample. Therefore, we developed an alternative procedure. This involves entering the d-spacing, ψ, and $\sin^2\psi$ values into a statistical program available on an IBM PC and performing a multiple regression of the d-spacing versus $\sin^2\psi$ and $\sin 2\psi$.

These measurements possess errors of two different types: counting statistics and regression fit errors. The counting statistics error represents the confidence of the data points. The regression fit errors show how closely the stresses in the material fit equation 3.3. Therefore, deviations of the goodness of fit for the counting statistics errors are indicative of shear stresses, grain size, and/or preferred orientation effects.

3.4 Summary

Understanding the role of residual stresses in materials is a crucial fact for improving the properties of the finished products. X-ray diffraction is a reliable technique that provides insight into the residual stresses developed in a device/material. While alumina has been studied in various structures using x-ray diffraction, silver-palladium metallization is a new material to be investigated in this field.

Chapter 4

TIME DOMAIN REFLECTOMETRY

4.1 Introduction

The purpose of the proposed research is to determine if hybrid processing induces residual stresses into thick film circuits and if changes in the electrical performance resulting from these stresses are significant. While the x-ray diffraction technique can determine changes in stresses, a measuring technique is necessary to determine if electrical changes can be measured and modeled. Two factors are involved in choosing the technique to make electrical measurements: simplicity and modeling capability. The technique satisfying these two criteria is Time Domain Reflectometry (TDR) technique. Since a wideband coplanar probe is under study, TDR provides the capability of rather simple measurements to characterize the electrical properties of the device. In addition, the TDR output trace can be modeled providing a way to compare traces by a physical model instead of just changes in voltage.

4.2 Description of Time Domain Reflectometry

This section describes the characterization of hybrid thick film structures at high frequencies up to a few gigahertz. Time domain measurement techniques can be applied to characterize and model thick film printed components as well as thin film deposited components over the frequency range from DC to a few GHz ($\approx$ 10 GHz).

4.2.1 Concept of The Time Domain Reflectometry Technique

The component or structure under test may be a segment of a transmission line (in the case of transmission line characterization), or a printed or deposited component located on a transmission line path. In the TDR method, the reflection from the component's input port is observed as a response waveform and is used to calculate the reflection transfer function of the input port of the component under test. This information can be used at a later time to model the desired component/structure by fitting the measured data to a physically based model.

TDR provides relevant information about discontinuities in a transmission system - information important in the modeling process. When an incident pulse in a TDR setup encounters a discontinuity, a fraction of the pulse is reflected. The magnitude and polarity of the reflected pulse depends upon the type of discontinuity. Figure 4.1 shows how the TDR reflection waves are generated. The waveform dips, peaks, oscillations, and relaxations of the TDR response are recognized as reflections caused by distributed and/or lumped discontinuities on the transmission line path. Utilizing the results of the TDR study on ideal components, as well as the physical nature of the structure, a model for the structure can be determined [31].

Figure 4.2 illustrates a TDR setup. A step-like pulse generated by a tunnel diode is transmitted down a precision line via a feed-through sampler. The pulse generator used is a tunnel diode with spectral contents covering a wide band of frequencies exceeding 10 GHz. The waveform reflected from the input port of the device under test (DUT) is observed as the

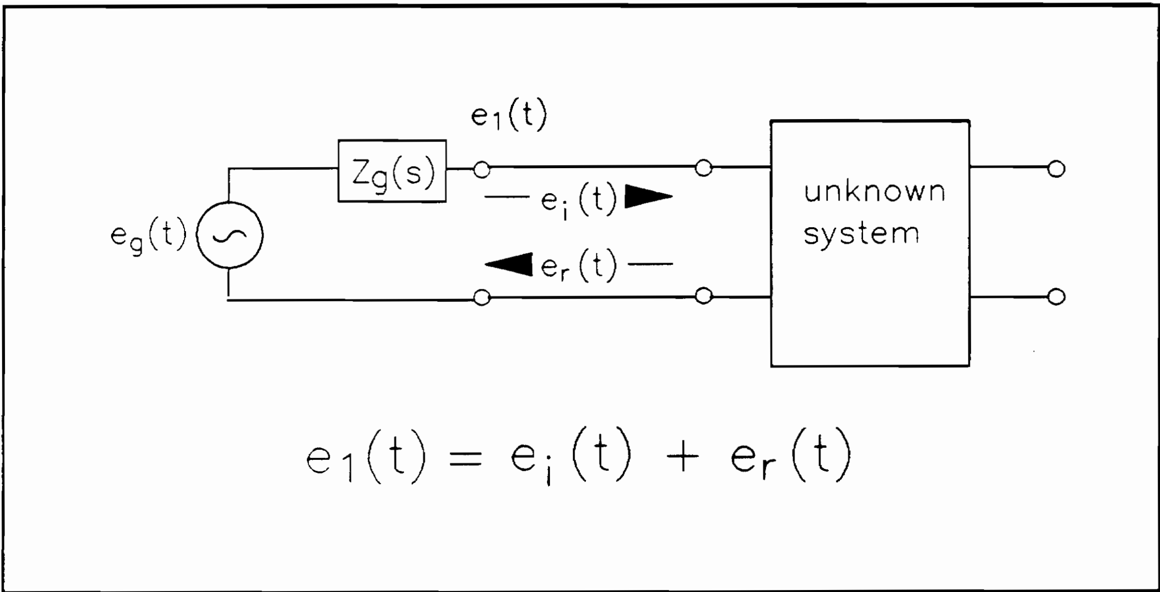

Figure 4.1: Diagram of Incident and Reflected Wave on Unknown System [30].

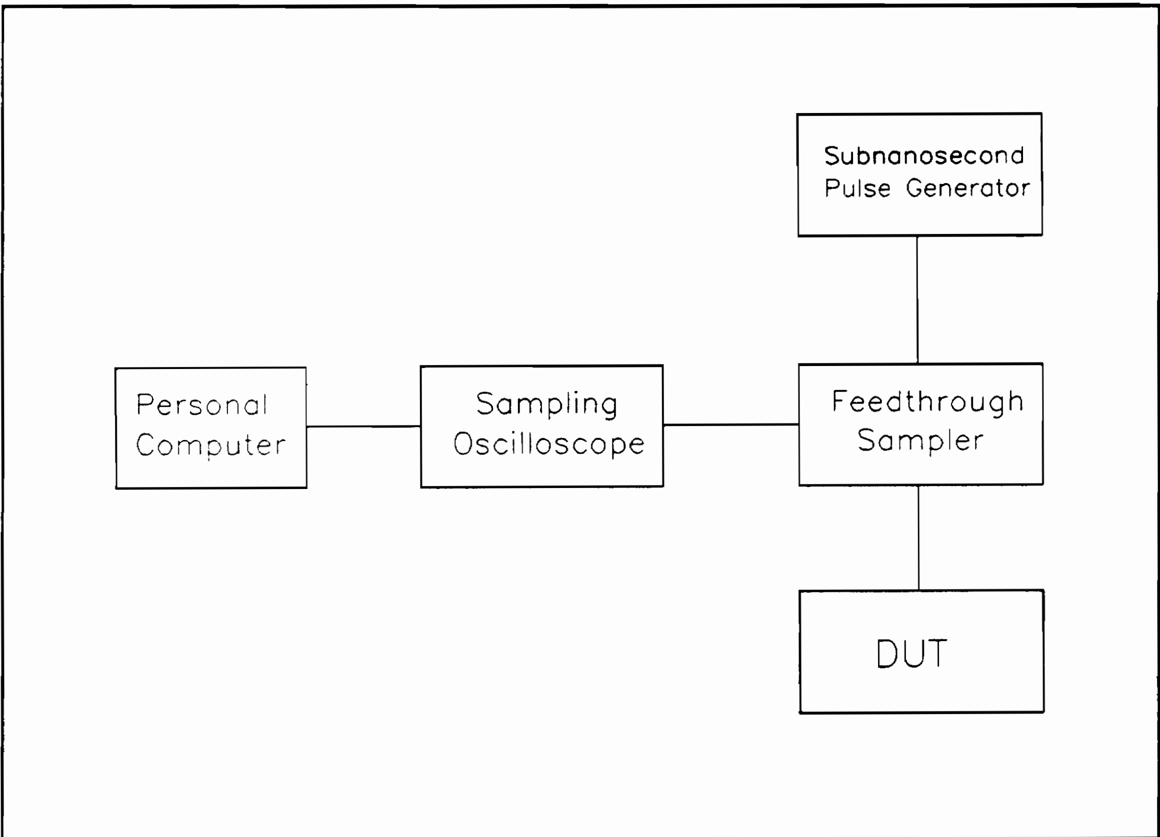

Figure 4.2: Setup of TDR Work Station

response waveform on a digital oscilloscope interfaced to a personal computer. The observed reflected waveform contains the necessary information (the incident reference waveform and the impulse response of the probe) to determine characteristics of the device under test such as the reflection coefficient.

In order to measure the reflection coefficient $\rho(j\omega)$, two waveforms are acquired. The response waveform $v_{resp}(t)$ is the reflection from the structure terminating the line. The reference waveform $v_{ref}(t)$ is the negative of the reflection from a short circuit located in front of the component/structure. A copper wedge is used to implement the required short. A nearly ideal short is required to eliminate any source of error. Using both $v_{resp}(t)$ and $v_{ref}(t)$, the termination's impulse response, h(t), can be shown to be

$$v_{resp}(t) = v_{ref}(t) * h(t) \tag{4.1}$$

where (*) denotes the convolution operation. The two acquired waveforms are then transformed into the frequency domain using the Fast Fourier Transform (FFT). Given equation 4.1,

$$h(t) = F^{-1}\left(\frac{F(v_{resp}(t))}{F(v_{ref}(t))}\right) \tag{4.2}$$

$$= F^{-1}[h(j\omega)] \tag{4.3}$$

The reflection coefficient $\rho(j\omega)$ is computed as the ratio between the two Fourier Transforms,

$$\rho(j\omega) = \frac{v_{resp}(j\omega)}{v_{ref}(j\omega)} \tag{4.4}$$

where $v(j\omega) = F(v(t))$. This function can be used to represent the device in the frequency domain.

4.2.2 Previous TDR Research Conducted on Coplanar Probes

As indicated in Chapter 2, the wideband coplanar probe is an adaptor for test equipment used to measure the TDR response of transmission lines. However, to understand its ef-

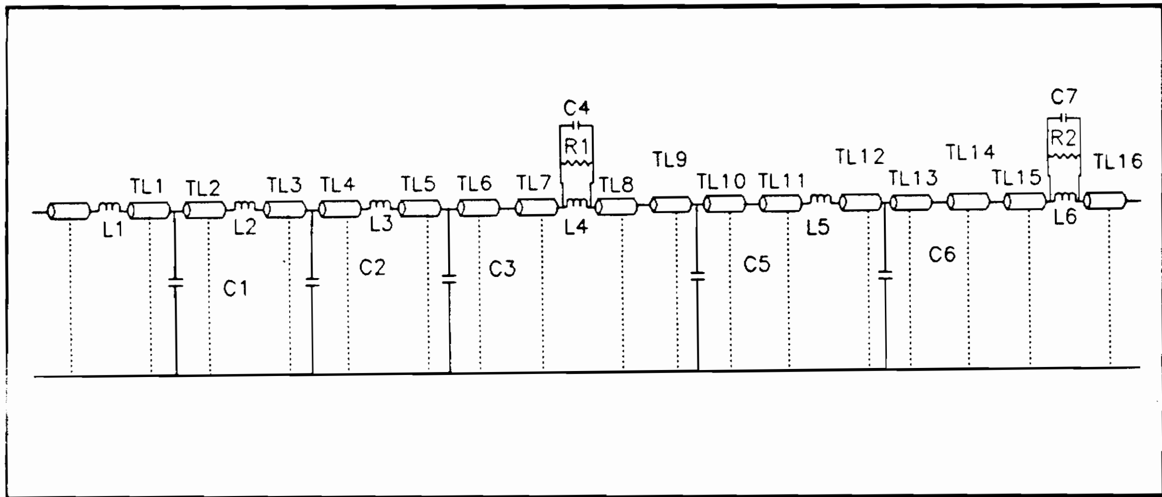

Figure 4.3: Network model of the probe [17].

Resistors		**Inductors**		**Capacitors**		**Transmission Lines**		
Number	**Value (Ω)**	**Number**	**Value (pH)**	**Number**	**Value (pF)**	**Number**	**Delay (ps)**	**Resistance (μ)**
R1	14.0	L1	25.5	C1	0.044	TL1	9.25	54.20
R2	10.0	L2	195.6	C2	0.010	TL2	9.15	46.00
		L3	66.0	C3	0.026	TL3	13.25	51.38
		L4	89.5	C4	0.015	TL4	19.10	51.37
		L5	139.0	C5	0.010	TL5	25.20	49.50
		L6	132.0	C6	0.100	TL6	10.00	47.00
				C7	0.035	TL7	24.50	52.00
						TL8	31.00	52.60
						TL9	3.50	53.00
						TL10	29.50	51.80
						TL11	40.50	53.90
						TL12	24.40	49.00
						TL13	5.80	48.50
						TL14	19.60	52.00
						TL15	7.50	50.50

Figure 4.4: Model Circuit Components and Respective Values [17].

fect on other TDR measurements, the device itself must be tested and modeled. This was achieved by Muthukrishnan, et. al. [17] using a modified version of the Transient Circuit Analysis Program (MTCAP). The model is shown in Figure 4.3 while the corresponding component values are given in Figure 4.4. This model shows a close correlation to the experimental results. The ideal representation for the probe would be a single transmission line with a 50 Ω impedance and some delay in the signal. However, the manufacturing process produces a probe that is modelled with a combination of transmission lines, resistors, inductors, and capacitors. The passive components, such as resistors, capacitors, and inductors, represent significant discontinuities in the transmission system, while the transmission lines have impedances approximately the same as ideal with some delay.

4.3 Measuring Electrical Properties of Coplanar Probes

4.3.1 TDR Measurements on Coplanar Probes

Using the test set-up described above, the electrical characteristics of the coplanar devices can be tested by three measurements: open circuit, short circuit, and matched impedance. During the open circuit test, the device was left disconnected on the opposite end from the connector. During the short circuit test, a copper wedge was attached to this end of the device. For the matched impedance measurement, a transmission line with nearly the same impedance is connected to the device under test. During each measurement, the observed reflected waveform is saved in a disk file on the computer for later comparisons and further analysis. Examples of the open circuit and short circuit measurements are shown in Figure 4.5.

4.3.2 Modeling of Time Domain Reflectometry Measurements

The disturbances in the TDR trace represent discontinuities in the transmission system where part of the incident wave is reflected. By observing the general shape of the waveform

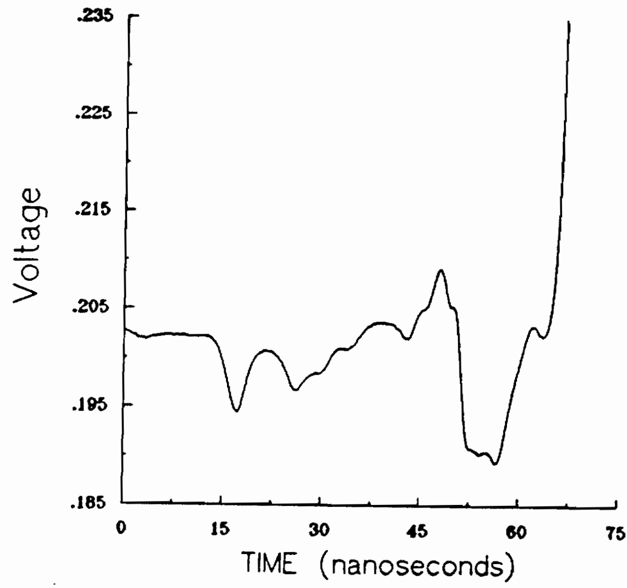

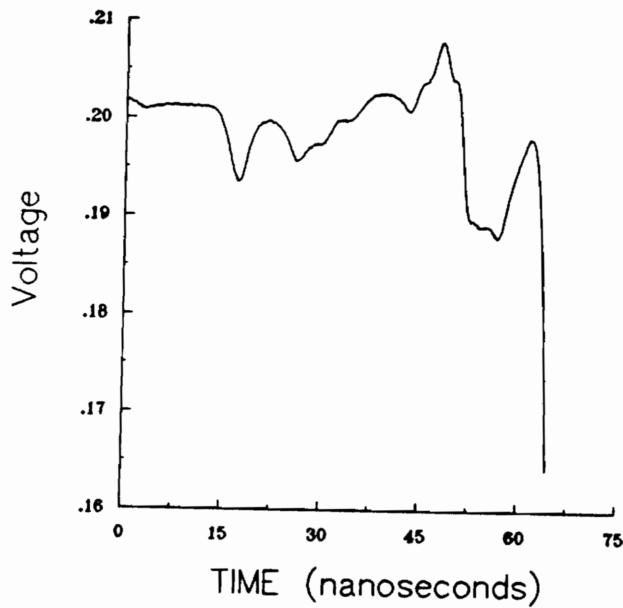

Figure 4.5: TDR Measurements on Probe: (a) Open Circuit (b) Short Circuit.

and the magnitude of the reflection, each discontinuity can be modeled as lumped and/or distributed elements. These models become particularly crucial when comparisons of various traces are necessary.

TDR offers a unique feature in the process. Because the technique is based on time domain, discontinuities can be dealt with one at a time, in the order of their physical location away from the launch end. Therefore, once the model component for a discontinuity is selected, changing the model components of later discontinuities does not affect the response waveform of earlier times. As a result, the modeling process involves dealing with only one discontinuity at a time [32].

Utilizing the results of the TDR study on ideal components, as well as the physical nature of the structure, a model for the structure can be determined. Each discontinuity may be modeled as a single element such as a capacitor or a combination of elements such as a resistor, capacitor, and inductor in series or shunt combination. The structure may be a single layer or multi-layer structure.

With the availability of the initial, physically based electrical network model and the reference waveform, the computer simulation can be started. The initial network model is used in the Modified Transient Circuit Analysis Program, MTCAP, to simulate the component under test. Using the acquired reference waveform as the excitation, a simulated TDR response waveform is computed as the reflected transient response of the network at its input port. Finally, The simulated response is then compared with the measured TDR waveform and the value of the different components in the model are adjusted, in an iterative fashion until a favorable match between the two waveforms is achieved.

4.4 Summary

This chapter has outlined the electrical testing technique of Time Domain Reflectometry. A previous TDR model for the coplanar probe has also been presented. Along with the general details of the TDR set-up and experimentation, a procedure for modeling the transmission

system was presented.

Chapter 5

MATERIALS AND PROCEDURES

5.1 Introduction

While research on residual stresses in hybrid thick film circuits can cover a large number of topics, the research conducted in this thesis tries to simplify the many variables in the manufacturing of these circuits. In order to determine initial correlations, a fairly simple circuit is used. In addition, instead of using specialized techniques, standard thick film screen printing is used. By analyzing the combination of materials and manufacture technology, measurement techniques such as x-ray diffraction and time domain reflectometry can add insight into circuit design and fabrication.

5.2 Materials, and Manufacturing and Processing Procedures

The materials used for this research consisted of two items: ceramic substrates and thick film conductor paste. The substrates used were manufactured by Kyocera. They measured 1 x 1 x 0.025 inch (25.4 x 25.4 x 0.64 mm), and were made of 96% alumina. Table 5.1 lists some of the characteristics of this ceramic material. Dupont 6134 silver-palladium (Ag-Pd) conductor paste was used. The Ag:Pd ratio for the paste was 6:1 in weight percent [34].

The realization of a finished probe device requires several different procedures: thick film manufacture, laser scribing, and component annealing. Residual stress and TDR techniques were used at various steps in the process to determine the critical steps in which stresses were introduced into the probe.

The thick film manufacturing process involves three steps, namely: printing, drying, and firing. Printing was accomplished using an AMI Presco Model 435 screen printer. The 6134 paste was printed using a 325 mesh, 90°, 5 x 5 inch (127 x 127 mm) stainless steel mesh screen. A screen breakaway distance of 0.025 inch (0.64 mm) was used. After printing, the probes were placed under a laminar flow hood for 15 minutes to allow the paste to settle. The paste was then dried at 150°C for 15 minutes in a Blue M Model POM-206B-1 drying oven. Firing of the paste consisted of a firing cycle of 60 minute profile with 10 minutes at a peak temperature of 850°C in a BTU Explorer Model TQ 41436NY four zone belt furnace.

Laser scribing with an ESI Model 25 laser trimmer was used to cut the substrate to the final desired shape. Cuts were made approximately 0.100 in (2.5 mm) away from the metallization. Because of the thickness of the substrate, a line was scribed with the laser and the substrate was then separated by hand.

Two different procedures were used to anneal the component: a low temperature anneal and a high temperature anneal. The low temperature annealing was performed in the same furnace and under the same heating cycle as described for firing of the metallization

($\approx 850^oC$). The high temperature annealing process involved taking the sample to 1500^oC for 120 minutes and then slowly cooling it over a forty eight hour period in a C.M. Inc. Rapid Temperature furnace. These two particular annealing procedures were used to determine the feasibility of removing or reducing the stresses. The production temperature anneal represented a practical procedure that could be done in the manufacturing environment without major process modification or extra equipment. On the other hand, the high temperature anneal procedure attempted to remove stresses without consideration of the production environment.

5.3 Procedures for Residual Stresses Measurements

The residual stresses were measured with a Technology for Energy Corporation Model 1610 portable apparatus for residual stress (PARS). The apparatus is shown in Figure 5.1.

5.3.1 Alumina Substrates

For this research work, the (146) diffraction peaks from alumina were chosen as the internal strain gauges. Previous work [19,35] at VPI&SU indicated that these planes provided accurate results for stress measurements using x-ray diffraction. Diffraction from these planes occurs at 136.3^o 2θ using copper K_α x-rays [22]. For our experiments, the copper tube was operated at 37 kilovolts and 1.8 milliamperes. To measure the (146) peak on the position-sensitive proportional counter (PSPC), the 135° mounting bracket was used. The diffracted x-rays passed through a thin nickel beta filter before being detected by the PSPC. Because of the narrow peak produced by the alumina planes, an ADC conversion gain of 512 channels was used to provide the necessary resolution to detect small shifts in the peak.

During the experiments a round 3 mm collimator was used. Measurements were made at seven different ψ angles: ± 33, ± 22, ± 15, and 0 degrees ψ. At each of these angles, the goniometer was oscillated three degrees ($\pm$ 1.5^o in each direction) to help eliminate any

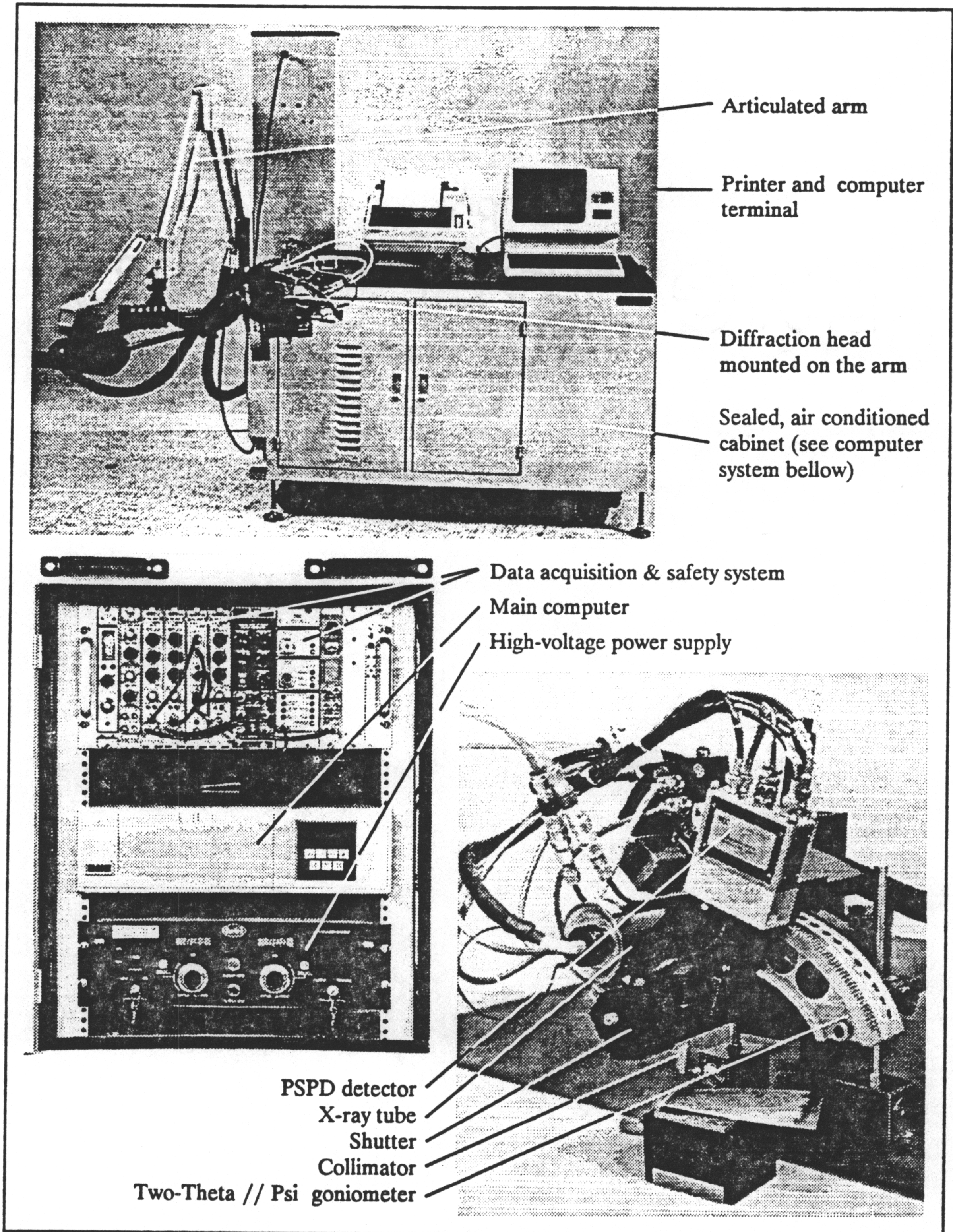

Figure 5.1: TEC Portable Apparatus for Residual Stresses. Photo Courtesy of Christophe Dehan.

effects of preferred orientation. Measurements were taken for a count time of 100 seconds for the ψ=0° angle. The measurement time for other angles was adjusted to account for changes in the x-ray path and absorption of the material. The total acquisition time was about fifteen minutes per stress data point.

The computer stored the PSPC output in a file. These scans have two distinct features besides the (146) diffraction peak. These two features are other diffraction peaks in bracket range and detector end effects. Both these effects are demonstrated in Figure 5.2 (a). The extra peaks in the bracket range occur at a lower 2θ than the (146) peak. Close examination of these extra peaks indicates that they are two overlapping peaks. This overlap prevents the computer from obtaining accurate stress values from these peaks. Although these peaks do not overlap with the reference peak, preferred orientation causes the heights of these two peaks to vary at different ψ angles. This result causes the TEC data analysis program to misinterpret the peaks and produce inaccurate values. The end effects are products of the electronics that cause the count levels at each end of the detector to appear as peaks. If the bracket angle is changed to place these "peaks" in the middle of the PSPC, no peak exists. To prevent any misinterpretation, the other peaks, which are irrelevant in the stress analysis, are removed with built-in TEC software so only the (146) peak remains. Figure 5.2 (b) shows the modified scan used for stress calculations.

The seven modified scans were then processed by a program that takes into account the background, Lorentz polarization, and sample absorption. Because the $K_{\alpha 1}$ and $K_{\alpha 2}$ peaks are clearly resolved, no K_α correction was used. From these modified peaks, the program used the top twenty percent of the peak to calculate a parabola by least square techniques and to determine the channel location of the top of the fit peak. This channel number relates to a 2θ value. From this 2θ value, a corresponding d-spacing was calculated using Bragg's law. This procedure was repeated for all seven ψ angles. Finally, these d-spacings were plotted versus $\sin^2\psi$. The slope and d-spacing intercept were determined by a linear regression of the data and the residual stresses were calculated. An example of these calculations is shown in Appendix ??. A typical d versus $\sin^2\psi$ plot for alumina is shown in Figure 5.3. Output from the program provided two sets of error analysis information.

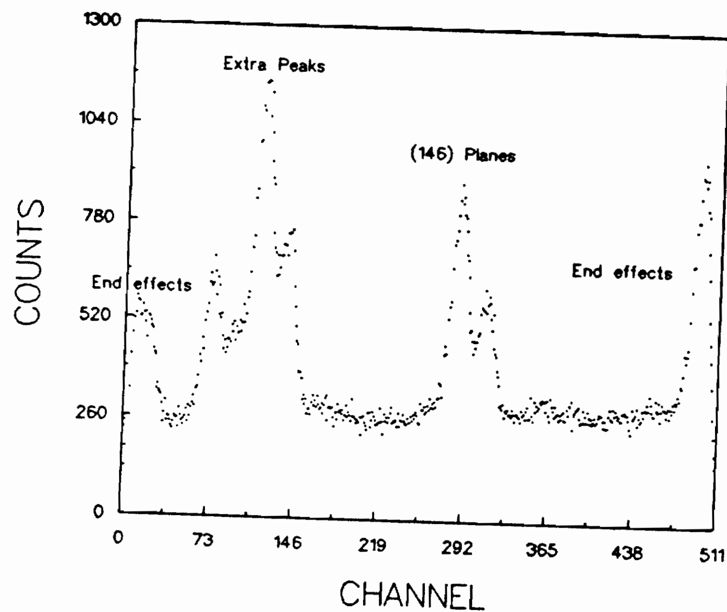

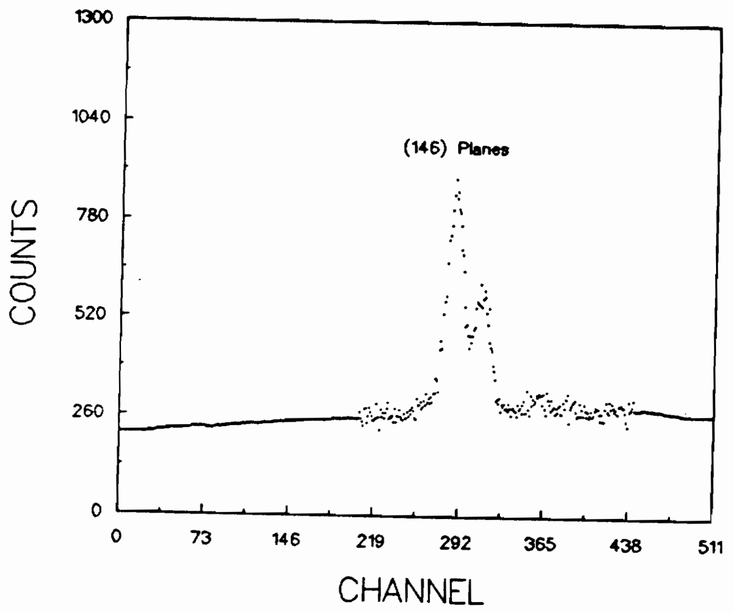

Figure 5.2: Alumina Diffraction Pattern: (a) Before modification. (b) After modification.

One was the counting statistic error. Based on the acquisition time and background, this value is related to the confidence level of each data point combined in the regression. The second error analysis number represents the deviation of the data from the linear regression line. High values for this statistic may indicate the presence of shear stress terms, grain size, and/or preferred orientation effects [21].

While qualitative trends can be observed by comparing the slope of the linear regression, the only way to compare quantitative results is to have accurate x-ray elastic constants. Fortunately, alumina is a widely used ceramic so research has been done to determine these constants. As mentioned in Chapter 3, the appropriate x-ray elastic constant is dependent on the crystallographic plane. A different constant is used for the (146) planes compared to other planes. X-ray elastic constants can be determined by two methods, experimentally or by calculation from single crystal constants. Tanaka, Yamamoto, and Suzuki [22] determined x-ray constants for different purities of alumina using several selected combinations of the diffraction plane and the x-ray wavelength. Their results are shown in Table 5.2. The second approach requires that the elastic constants for single crystals be known. Then for a given system of planes, the appropriate elastic constants can be calculated [21]. Calculations by Foster and Tontodonato [35] determined $E/(1+\nu)$ to be $40.3 * 10^{-6}$ psi ($2.78 * 10^{-9}$ Pa). This number was calculated for pure alumina and agrees within 20% of experimental values. We have chosen to use the results of Tanaka et. al. since the elastic constant value was determined for 96% alumina substrate. Since only 80% of the substrate by volume is alumina, there is a big effect of the 4 atomic percent glass content and this differentiation is vital.

Each set of experiments was performed five times to help reduce systematic experimental errors resulting from positioning at each location on the sample. Computer calculations were done on all five sets of data. Next, the five sets of seven d-spacings for each substrate location were entered into ABstat, a statistics package by AndersonBell [36], to allow for a multiple regression of the data. These additional computer manipulations enabled the data to be multiply regressed versus $\sin^2\psi$ and $\sin 2\psi$. From the coefficients obtained in the regression and the x-ray constants, the values for both the normal and shear stresses were

Table 5.1: Properties of 96% Alumina Substrate Material [33].

Flexural Strength	40 ksi	276 MPa
Young's Modulus	$50*10^3$ ksi	$3.45*10^5$ MPa
Coefficeint of Linear Thermal Expansion	$7.1 * 10^{-8}$/ °C	

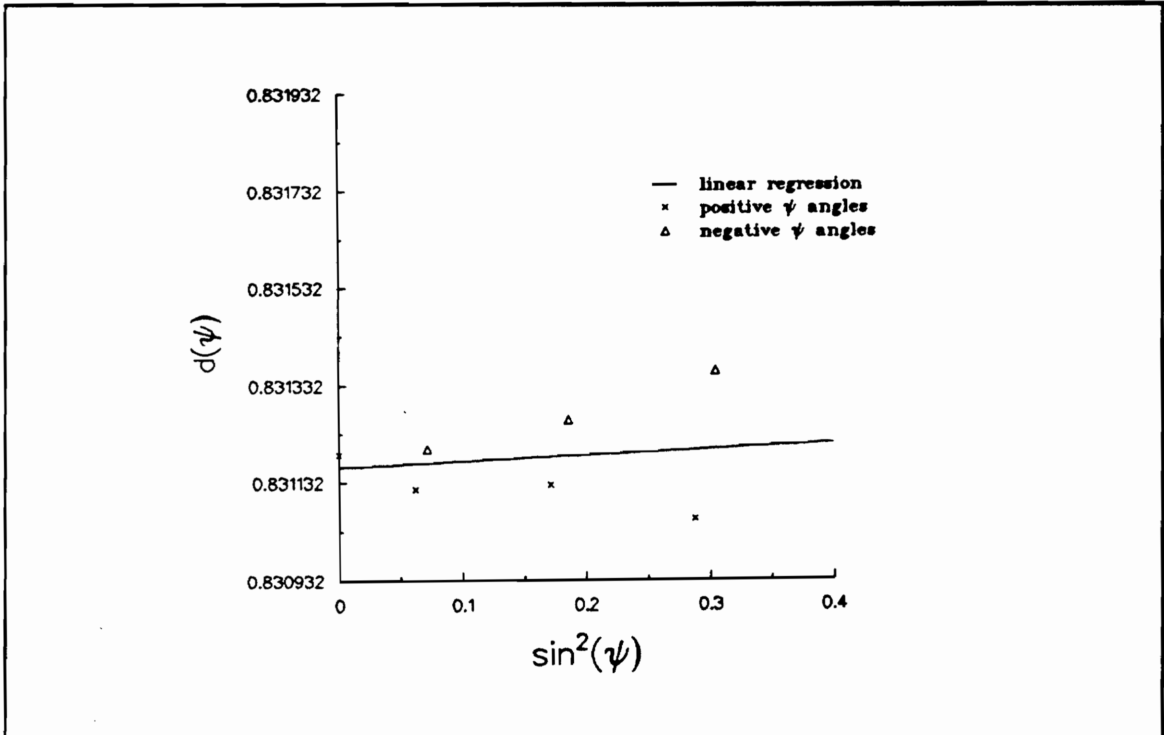

Figure 5.3: D versus $\sin^2\psi$ plot for Alumina.

calculated. The five repetitions and statistics also enabled us to test many possible groups of data for accuracy and precision as will be discussed in Chapter 6.

5.3.2 Silver-Palladium (Ag-Pd) Metallization

While information was found in the literature on available peaks in alumina, no published information was available for silver-palladium metallization. Therefore, preliminary experiments were necessary to determine if a diffraction peak was available at high Bragg angles and, if by using this peak, stresses could be calculated. Initial experiments showed an excellent peak existed at approximately 156° 2θ using chromium K_α radiation as illustrated in Figure 5.4. For these experiments, the chromium tube was operated at 35 kilovolts and 1.7 milliamperes. Calculations (shown in Appendix A) identified that the peak corresponds to the (222) planes of the silver-palladium alloy. To measure the peak with the PSPC, the 156° mounting bracket was used. The diffracted x-rays passed through a thin vanadium filter before being counted.

During the experiments, a round 3 mm collimator was used. Measurements were made at seven different ψ angles: ±35, ±22, ±15, and 0 degrees ψ. At each of these angles, the goniometer was oscillated two degrees (±1.0° in each direction) to help eliminate any effects of preferred orientation. Measurements were taken for a count time of 100 seconds for the $\psi = 0^o$ angle. As with the alumina measurements, the time at other ψ angles was adjusted to account for changes in the x-ray path and absorption of the material. Thus, a total acquisition time of the order of fifteen minutes for each stress measurement was required.

As described above for the alumina measurements, the peaks were stored in a file. The metallization peak did not have the extra peaks or end effects seen with the alumina so the scans were processed to account for background, Lorentz polarization, and sample absorption without modification. The K_α peaks were not as distinguishable as with the ceramic so built-in K_α correction was used for the silver-palladium peaks. The calculation for the peak channel position and related stress values followed the same procedure as above. An example of a regression of d-spacing versus $\sin^2\psi$ for the Ag-Pd metallization is seen in

Table 5.2: X-ray Constants for (146) Planes of Alumina [22].

Alumina (% Purity)	Elastic Constant $\frac{E}{1+\nu}$ ~~Ksi~~ Msi (GPa)
99	47.0 (324)
96	45.2 (312)
92	34.8 (240)

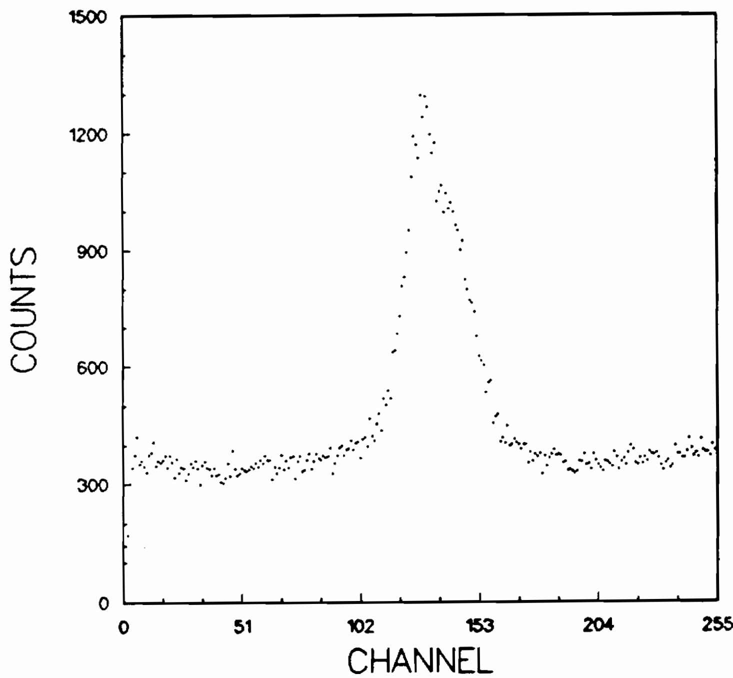

Figure 5.4: Silver-Palladium (222) Diffraction Peak.

Figure 5.5.

Since the x-ray elastic constants for the silver-palladium metallization are not available in the literature and experimental determination was not possible with current facilities, the only alternative for determining the elastic constants was to calculate the numbers based on single crystal values. Simmons and Wang [37] compiled a list of single crystal elastic properties from the literature. This list contained the elastic compliance matrices as well as reported calculated aggregate properties for silver, palladium, and silver-palladium alloy. Table 5.3 shows the compliance matrix for these three materials. From the compliance matrices, the Young's modulus and Poisson's ratio can be calculated using the Voigt average and the Reuss average techniques [21]. The Voigt average assumes equal strains across the material while the Reuss average assumes equal stresses. The true value of the elastic constant is in between these two averages. These resulting parameters as well as $E/(1+\nu)$ are shown in Table 5.4. Since the silver-palladium paste is 6:1 weight percent Ag:Pd, the Reuss and Voigt averages for the average of the silver from different sources and the silver-palladium alloy were combined and the mean value of $E/(1+\nu)$ was used. If this alloy indeed acts as bulk material then the error of this assumption is approximately ten percent. However if the alloy acts like a thin film, the stress values could be substantially different from calculated values.

5.4 Measuring Electrical Properties of Coplanar Probes

5.4.1 Measuring TDR Responses of a Coplanar Probe

Time domain reflectometry measurements were made using an HP Model 54120A Digitizing Oscilloscope Mainframe. The coplanar device was attached to the measuring device by an Omnispectra Inc. SMA End Launch Jack with modifications designed by VPI&SU researchers to fit our application. This connector converts from coaxial geometry to planar geometry. The center conductor on the device under test is soldered to the center conductor on the connector. Figure 5.6 illustrates this experimental set-up.

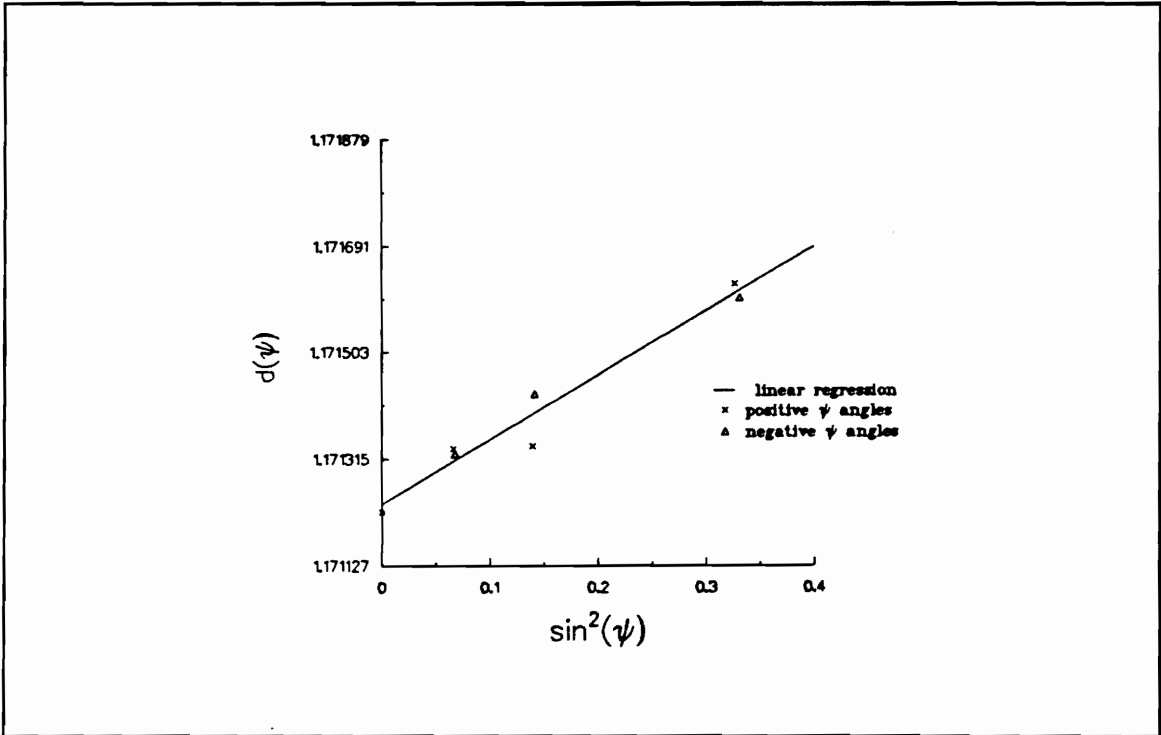

Figure 5.5: D versus $\sin^2\psi$ plot for Ag-Pd Metallization.

Table 5.3: Compliance Matrices of Materials [37].

Material	S_{11} (10^{-11} Pa)	S_{12} (10^{-11} Pa)	S_{44} (10^{-11} Pa)
Silver			
	2.320	−0.993	2.290
	2.286	−0.982	2.169
	2.254	−0.961	2.347
	2.226	−0.948	2.203
Silver−Palladium (93.78/6.22)			
	2.194	−0.941	2.079
Palladium			
	1.355	−0.591	1.399

Table 5.4: Elastic Constants for Metallization materials [37].

Calculations Using Voigt Average			
Material	Young's Modulus (E) 10^7 psi (10^{11}Pa)	Poisson's Ratio (ν)	$\frac{E}{1+\nu}$ 10^7 psi (10^{11}Pa)
Silver			
	1.266 (0.873)	0.354	0.935 (0.645)
	1.325 (0.914)	0.353	0.980 (0.676)
	1.250 (0.862)	0.357	0.921 (0.635)
	1.314 (0.906)	0.351	0.973 (0.671)
Silver–Palladium (93.78/6.22)			
	1.380 (0.952)	0.351	1.022 (0.705)
Palladium			
	2.117 (1.460)	0.373	1.541 (1.063)

Calculations Using Reuss Average			
Material	Young's Modulus (E) 10^7 psi (10^{11}Pa)	Poisson's Ratio (ν)	$\frac{E}{1+\nu}$ 10^7 psi (10^{11}Pa)
Silver			
	0.998 (0.688)	0.385	0.721 (0.497)
	1.027 (0.708)	0.386	0.741 (0.511)
	1.009 (0.696)	0.384	0.729 (0.503)
	1.038 (0.716)	0.382	0.751 (0.518)
Silver–Palladium (93.78/6.22)			
	1.069 (0.737)	0.385	0.771 (0.532)
Palladium			
	1.692 (1.167)	0.399	1.209 (0.834)

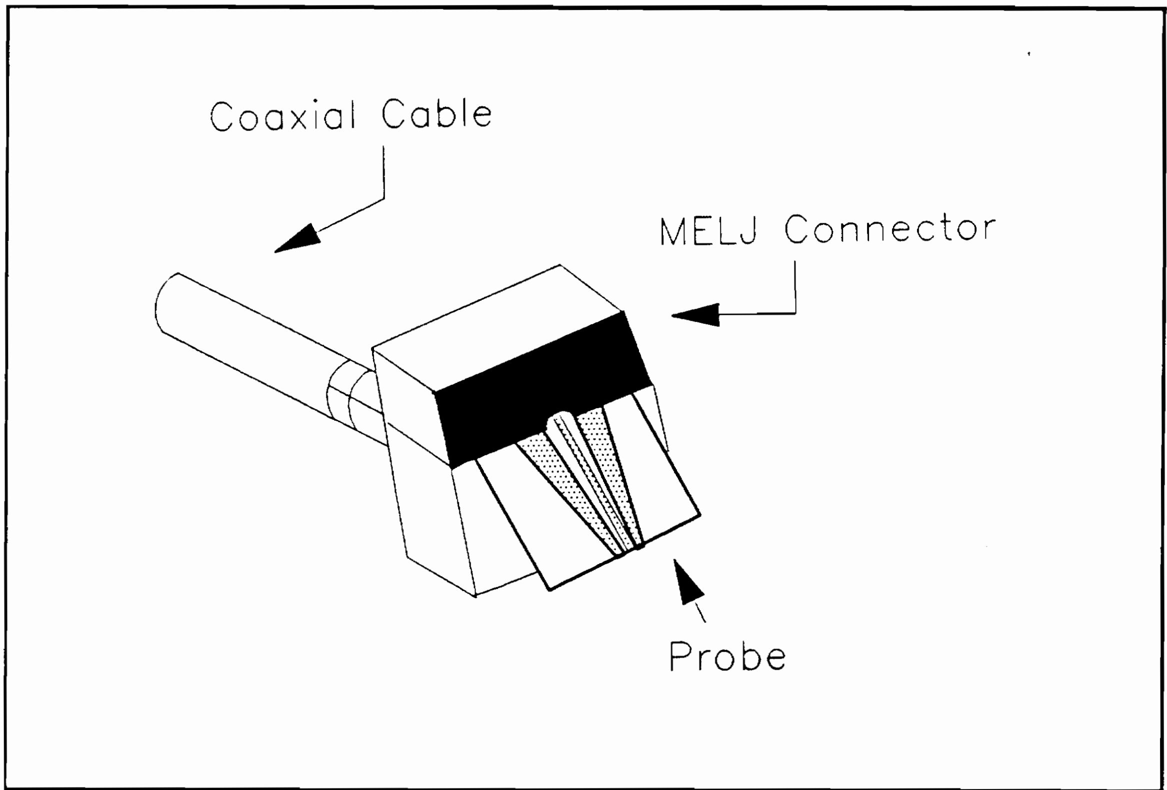

Figure 5.6: Drawing of TDR Setup with Probe.

Electrical characteristics of the coplanar devices were tested by two measurements: open circuit and short circuit. During the open circuit test, the probe was left disconnected on the end opposite the connector. During the short circuit test, a copper wedge was attached to that end of the probe. The observed reflected waveform was saved in a disk file on the computer for later comparison and analysis after each measurement. Five hundred points were taken at 150 picosecond intervals. Examples of the open circuit and short circuit measurements are illustrated in Figure 5.7.

5.4.2 Modeling of TDR Responses

To allow for direct comparison of two waveforms, the TDR traces need to be modeled using the initial network model presented by Muthukrishnan et. al. [17] using the Modified Transient Circuit Analysis Program, MTCAP. A simulated TDR response waveform can be computed as the reflected transient response of the network at its input port. The simulated response is then compared with the measured TDR waveform and the values of the different components in the model are adjusted until a favorable match between the two waveforms is achieved.

5.5 Correlation of Materials Processing with Residual Stresses and Electrical Measurements

All of the techniques described above outline individual aspects of the thick film manufacture, residual stress measurement, and TDR procedures. However, to determine the relationship between stresses and electrical properties in hybrid thick film circuits they must be combined. This section outlines the combination of these procedures to determine the correlation between these stresses and the corresponding electrical characteristics.

The first set of experiments was used to characterize the starting conditions of the substrate. Three bare substrates were characterized. Five independent measurements were

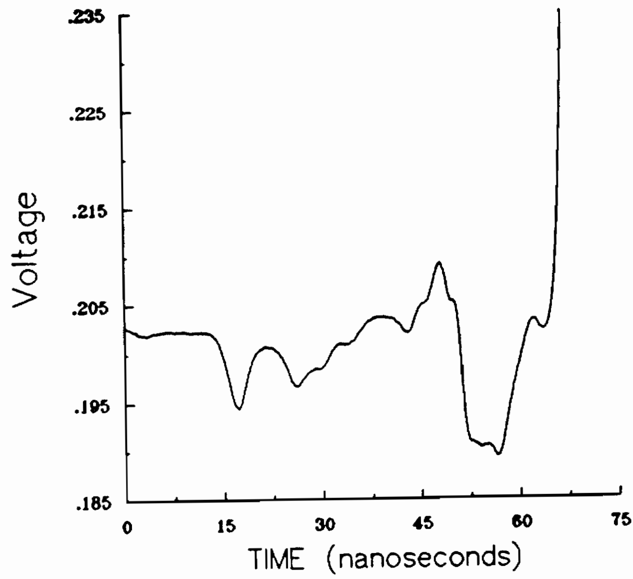

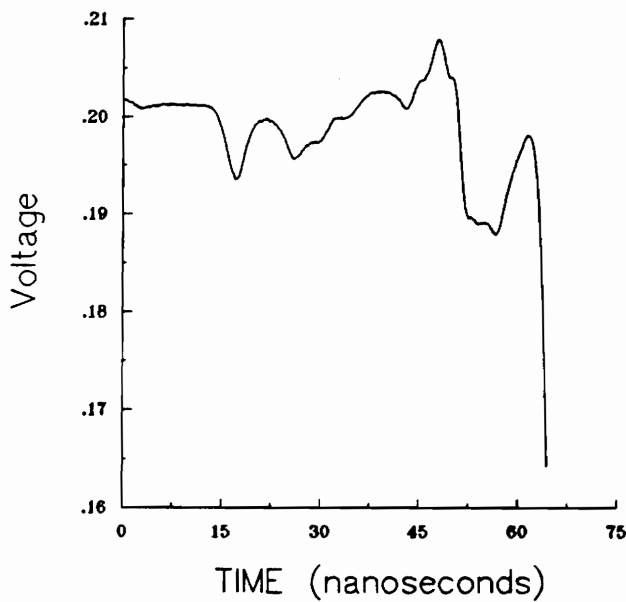

Figure 5.7: TDR Measurements on Probe: (a) Open Circuit (b) Short Circuit.

made at three different locations in two orthogonal directions as shown in Figure 5.8. This resulted in a total of thirty stress measurements incorporating 210 individual x-ray diffraction peaks per substrate.

After characterizing the bare substrates, the same three samples were processed along different paths to determine how the various production steps affect residual stresses. Sample 1A proceeded through the entire process (printed, fired, and laser cut). Stress measurements were made after firing and after laser cutting. Sample 2A was only laser cut, while sample 3A was only fired. Stress measurements were made after each step in the same manner as with the bare substrates. Figure 5.9 shows the processing steps of the three samples.

Next, two different annealing steps were tested to determine how each affected the state of stress in the substrate. The production temperature annealing procedure consisted of processing the sample through the standard 850°C, one hour profile twice and measuring stresses after each firing. Sample 1A was used for this experiment. The high temperature annealing procedure consisted of heating the substrate to 1500°C for 10 hours, holding this temperature for 2 hours, and then very slowly cooling it to room temperature over a period of 24 hours. Because this high temperature (1500°C) anneal would exceed the temperature at which the metallization was stable, this experiment was performed on sample 2A which was a bare, but laser cut, substrate. Five stress measurements were made after each anneal at a single location on the back of the circuit.

Stresses were also investigated in the metallization. Stress measurements were made on two different laser trimmed probes. The location of these measurements is shown in Figure 5.10.

5.6 Summary

This chapter presented the materials and procedures used to investigate the role of residual stresses in thick film circuits. Along with characteristics of the alumina substrate and the

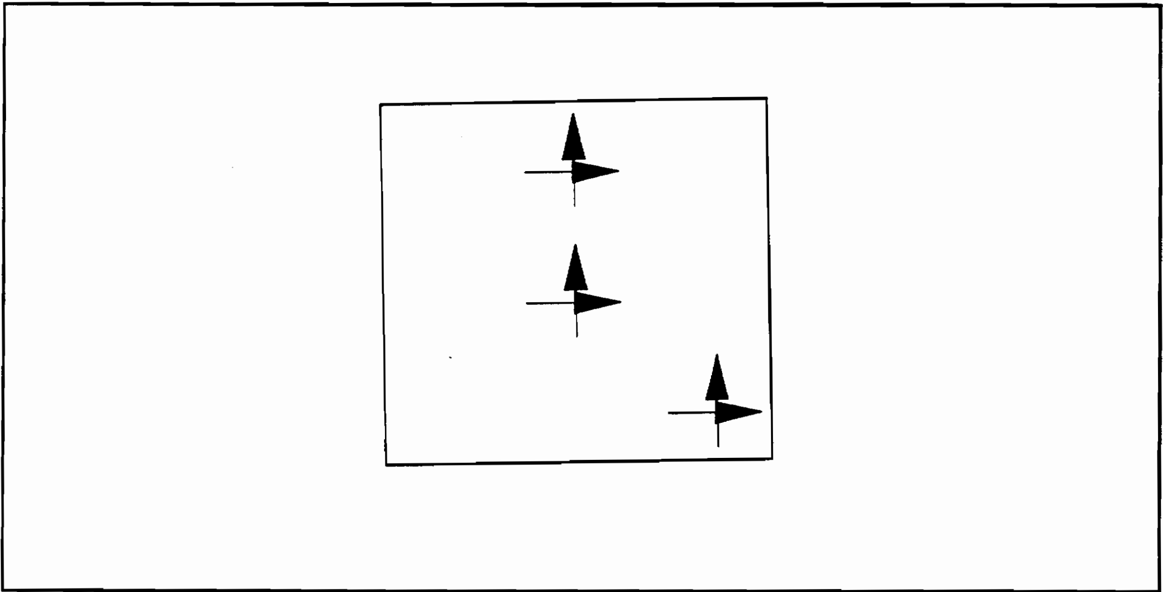

Figure 5.8: Location and Direction of Stress Measurements on Substrate.

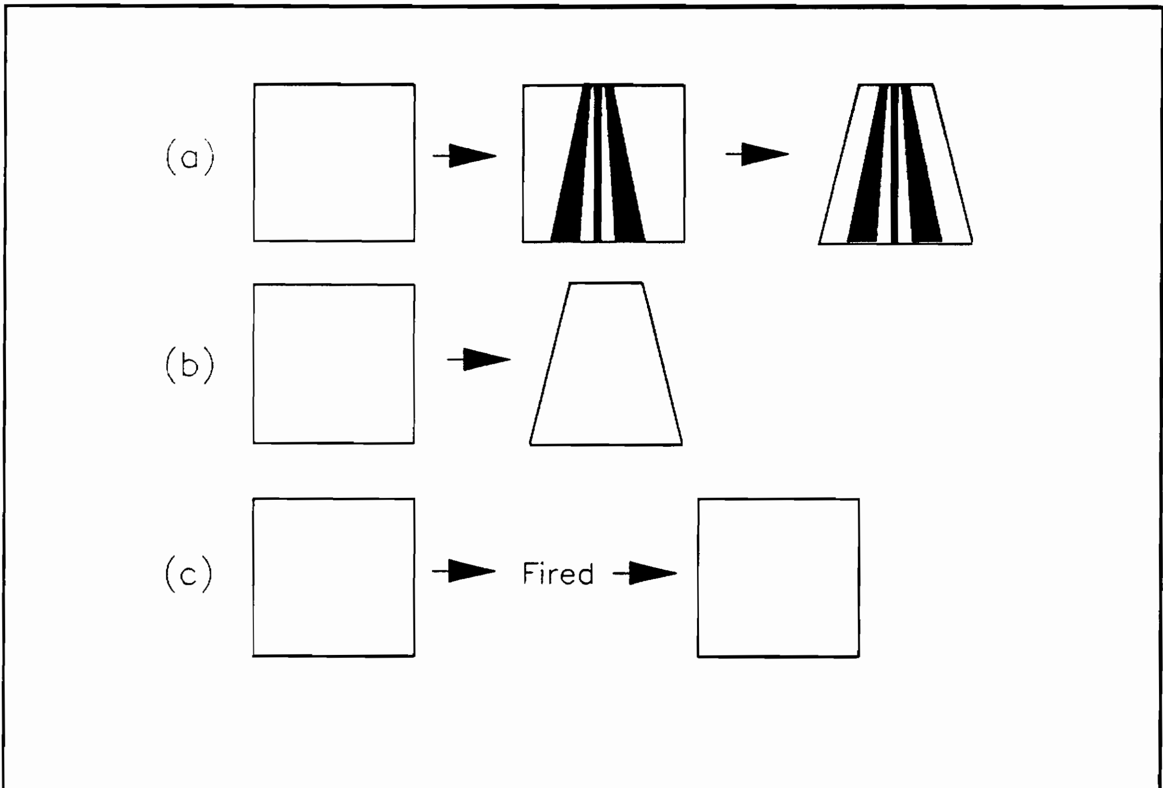

Figure 5.9: Processing Steps of Substrate: (a) Sample 1A, (b) Sample 2A, and (c) Sample 3A.

Ag-Pd paste, the techniques used for manufacture of the coplanar probe were introduced. Details on the analytical techniques of stress and TDR measurements were also reported. Finally, the various combinations of manufacture and analytical techniques were presented.

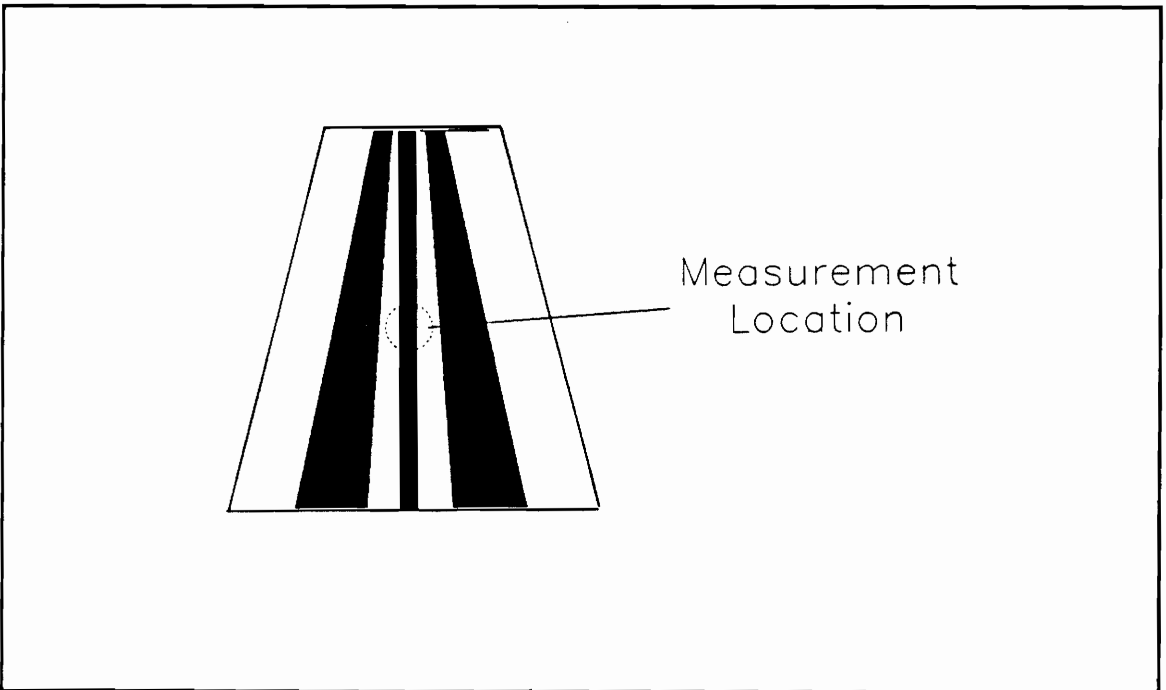

Figure 5.10: Location of Stress Measurements on Metallization.

Chapter 6

RESULTS AND DISCUSSION

6.1 Introduction

To understand the effect of processing on the electrical properties of a hybrid circuit, an intermediate tool was necessary. This tool was the measurement of residual stresses. This chapter outlines the results obtained in the investigation of the relationship between processing and residual stresses in both the ceramic substrate and the metallization. These results are then combined with the TDR measurements to determine which electrical changes may be attributed to the various processing parameters.

6.2 Residual Stresses in the Ceramic Substrate

6.2.1 Characterization of Bare Substrates

This first set of experiments played an important role in determining whether residual stresses were present in the starting material or were induced by various processing steps. It was essential to determine:

1. if a substrate has a stress gradient at different locations,
2. if there are variations in stresses between the two orthogonal directions, and
3. the reproducibility and precision of the residual stress measurements.

The results of each set of five stress measurements were organized in different groups representing the possible combinations.

Group A – same location/same orientation
Group B – same location/both orientations
Group C – different locations/same orientation, and
Group D – different locations/both orientations.

Each set was statistically analyzed to determine if there was a correlation between location, orientation, and the different stress values. A multiple regression of the d-spacing versus $\sin^2\psi$ and $\sin 2\psi$ was performed on each above group. The sample space ranged from 35 d-spacings in Group A to 210 d-spacings in Group D. The results of this analysis on each group showed that although the first three groups have slightly different mean stress values, the coefficients of the multiple regression of $\sin^2\psi$ and $\sin 2\psi$ had the highest level of confidence when the data from all three locations and both orientations were combined. Table 6.1 summarizes the normal and shear stresses measured in the bare substrates.

The results show that, based on in all ninety stress measurements on the bare substrates, the coefficient σ_{11} of equation 3.3 is not statistically significantly different from zero. Small shear stresses (σ_{13} orσ_{23}) were observed in all three substrates. In addition, repetitions of these experiments showed that measurements were statistically repeatable, with d-spacing errors of $20 * 10^{-6}$ Å, and were consistent over the entire face of each sample. This indicates that any systematic errors caused during the mechanical alignment and positioning of the sample were eliminated by repeating the test five times.

These results indicate that, stress-wise, the bare substrates are homogeneous and that there is no statistical difference between the two orthogonal directions. These two facts have

important production implications. First, since the bare substrate is homogeneous when comparing the center, the edge, and the corner, circuit designers do not need to take into account the physical placement of the components. Second, the fact that the two orthogonal directions are the same implies that when using a square substrate in either orientation (0° or 90°), the circuit should not see varying stress values. This observation also means printed components laid out parallel or perpendicular to one another should be affected in the same manner by any stresses developed on the substrate.

6.2.2 Characterization of Processing Steps

After characterizing the bare substrates, the next step was to determine how the production steps affected the residual stresses. Firing alone has no effect on the substrate stresses as indicated in Sample 3A. This sample, within statistical accuracy, had the same normal and shear stresses after firing without paste as were present in the bare, unfired substrate (2.62 $\pm$ 4.57 ksi (18.1 $\pm$ 31.5 MPa)).

The stresses that developed in Sample 1A as it was processed through a normal production cycle are summarized in Table 6.2. The bar graph in Figure 6.1 shows the trend of the normal and shear stresses. The increase in stress from the bare to print/fired state is attributed to the interaction between the conductor paste and substrate. As was shown by Sample 3A, the stresses developed during printing/firing are not a result of the thermal treatment of the substrate. While manufacturers are striving to decrease the mismatch between the thermal coefficient of linear expansion (TCE) of the substrate and thick film pastes, the values are still very different [34]. The TCE of Ag-Pd has not been determined by the manufacturer but should be close to the value for silver of $19.6 * 10^{-8}/^oC$ [38]. This represents almost a 3:1 difference between substrate and metallization. If one assumes the strong adhesion of the metallization to the substrate occurs at the 850°C firing temperature, then on cooling this difference in TCE causes the metallization to shrink more than the alumina putting the metallization in tension. The top surface of the substrate will be in compression resulting in an equal tensile stress on the back. This will be discussed further

Table 6.1: Normal and Shear Stresses in Three Bare Substrates.

Substrate	Normal Stress ksi	Normal Stress (MPa)	Shear Stress ksi	Shear Stress (MPa)
1A	0.3 ±2.2	(2.2 ±15.0)	−2.6± 0.3	(−17.7± 2.3)
2A	0.3 ±2.2	(2.1 ±14.9)	−3.9± 0.3	(−26.8 ±2.3)
3A	−0.7± 4.4	(−4.6± 30.5)	−4.5± 1.0	(−31.2 ±7.1)

Table 6.2: Normal and Shear Stresses as Probe 1A is processed.

Processing Step	Normal Stresses ksi	Normal Stresses (MPa)	Shear Stresses ksi	Shear Stresses (MPa)
Bare	0.3 ±2.2	(2.2 ±15.0)	−2.6± 0.3	(−17.7±2.3)
Printed/Fired	5.6 ±1.8	(38.3 ±12.5)	−4.2± 0.3	(−26.8±2.3)
Laser Cut	15.6±2.4	(107.0±16.7)	−6.8± 0.4	(−31.2±7.1)

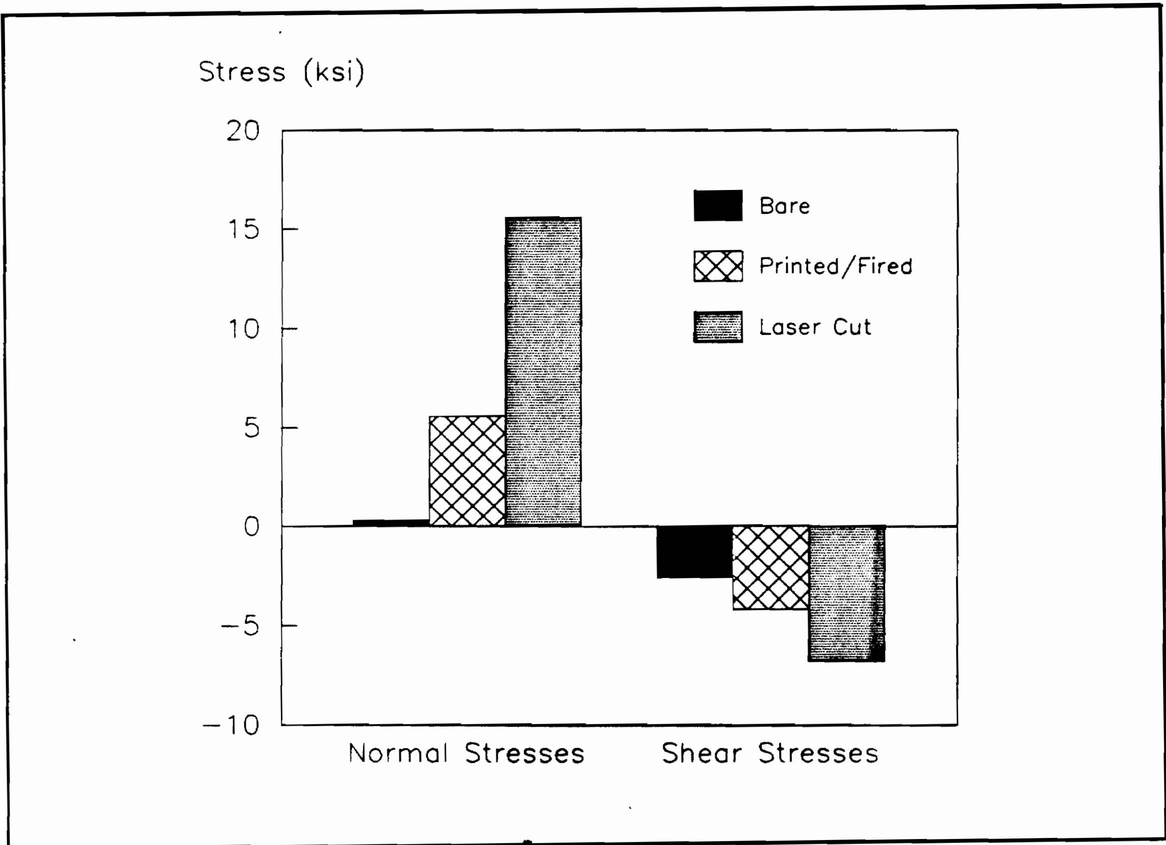

Figure 6.1: Comparison of Normal and Shear Stresses for Processing

in section 6.3.

The large tensile normal stresses seen in the fully processed sample (1A) represent significant residual stresses. The final normal stress value of 15.6 ksi (107.6 MPa) is roughly 40% of the estimated rupture stress of 40 ksi (276 MPa) indicated by the manufacturer. This value is significant because of the material strength properties of the alumina ceramic. Unlike ductile metals that have very reproducible yield and fracture stresses, brittle ceramics exhibit wide variations in their rupture stresses. These stresses are often described by a two or three parameter Weibull distribution. Figure 6.2 demonstrates such a distribution for Coors alumina rods of the same composition [35]. The 42.5 ksi rupture stress represents the value at which 50% of the samples would have shattered. Because the Weibull distribution is broad, the stresses measured in the finished probe represent a significant percentage of samples that will fail either in production or once small external stresses are applied. This decrease in overall stress resistance could prove important in packaging environments.

The role of laser trimming in producing these large stresses was confirmed by laser trimming a bare substrate to the same shape and size as the manufactured probe. Sample 2A showed significant tensile stresses of 12.6 ± 2.6 ksi (86.5 ± 17.9 MPa). While this value is slightly smaller than the fully processed probe, the experiment demonstrates two points. First since laser trimming was the only processing step, the resulting stresses may be attributed solely to this process. Second since the stress value is smaller than that found in the fully processed probe, it is suggested that the final stresses in the fully processed sample result from the combination of the two processing steps of firing and laser trimming.

6.2.3 Characterization of Annealing Steps

The tensile stresses observed in laser cut samples are expected to contribute significantly to device failures, and therefore must be removed or reduced. One method to relieve these stresses is by annealing. Two forms of annealing were tested: production temperature annealing and high temperature annealing. Table 6.3 summarizes the stresses measured using these two techniques. Figures 6.3 and 6.4 show the general trends of the normal and

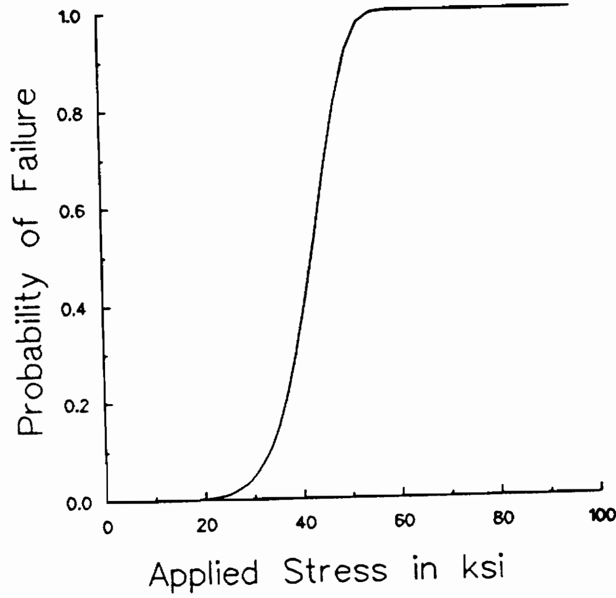

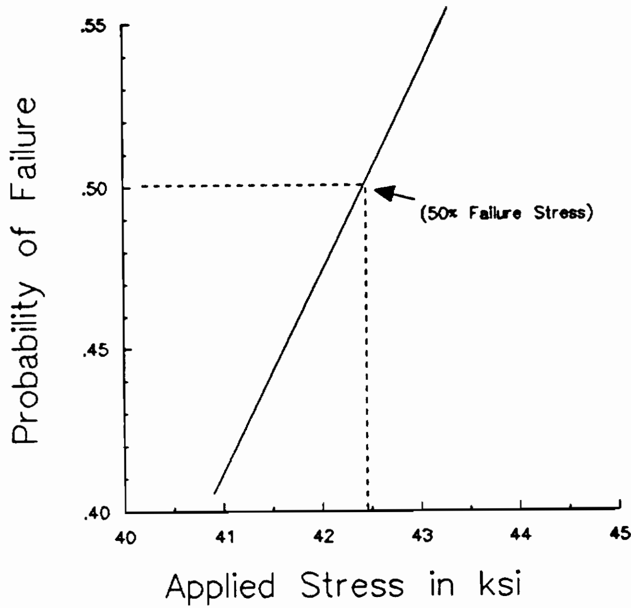

Figure 6.2: (a) Weibull Distribution for Coors Alumina [35] (b) Enlargement of middle section of graph to show 50% failure stress value.

shear stresses. For the production temperature anneal, the tensile normal stresses decrease with each firing while the shear stresses remain essentially constant. A linear regression of these data indicate that, if the stresses continued to be annealed at the same rate, the normal stresses in the substrate would be approximately zero after five post firings, as illustrated in Figure 6.5.

The lower part of Table 6.3 shows the results of the high temperature anneal (1500°C) on Sample 2A. During this anneal, the normal stresses and shear stresses are both reduced by about a factor of two. This implies that, although the stresses were not completely eliminated (probably as a result of thermal stresses from too rapid a cooling cycle), there was a significant effect in the reorientation of the stress ellipsoid which did not occur with the production temperature anneal described above.

Another fact that might have contributed to the different effect on the shear stresses is the presence of the metallization. The substrate tested at high temperatures was bare while the production temperature substrate had fired metallization in the probe pattern on it. The constraints caused by the presence of the metallization may prevent the ceramic from relieving stresses in some directions. Although it is beyond the scope of this thesis to examine the details of the mechanism of stress relaxation during annealing, it is clear from these two experiments that quite different processes are occurring during each anneal.

The production temperature annealing results suggest that stresses can be annealed out by post-firing. However, several problems exist with this alternative. First, processing each device through the production furnace four or five extra times would be costly. Second, additional firings cause changes in the characteristics of pastes already on the substrate. Finally, since this anneal does not remove the shear stresses, there remains some uncertainty concerning the role of such stresses in the lifetime of the finished product.

The single high temperature annealing experiment indicates that such anneals reduce, but do not fully eliminate, both the normal and the shear stresses in the laser cut samples. Peak temperatures and cooling rates could be modified to determine the optimal combinations for eliminating stresses. Since this technique requires temperatures almost twice

Table 6.3: Normal and Shear Stresses for Different Annealing Cycles.

Condition	Normal Stresses ksi (MPa)	Shear Stresses ksi (MPa)
Sample 1A		
Processed	12.0±3.0(83.0±20.7)	−5.1±0.5(−35.0±3.2)
Postfired 1	9.2±2.4(63.5±16.8)	−5.1±0.4(−35.2±2.6)
Postfired 2	7.2±4.2(49.6±29.2)	−4.5±0.7(−31.1±4.6)
Sample 2A		
Processed	12.6±2.6(86.5±18.0)	−6.1±0.4(−42.1±2.8)
Anneal 1500°C	6.4±2.4(43.8±16.3)	−1.9±0.4(−13.4±2.5)

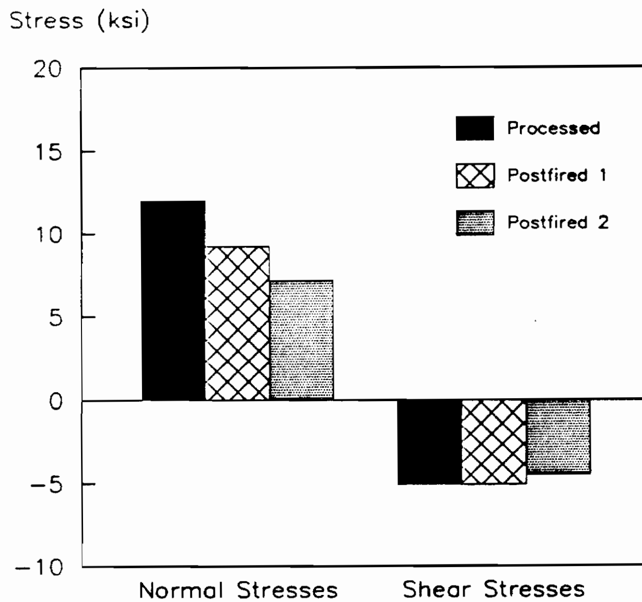

Figure 6.3: Comparison of Normal and Shear Stresses for Low Temperature Anneal.

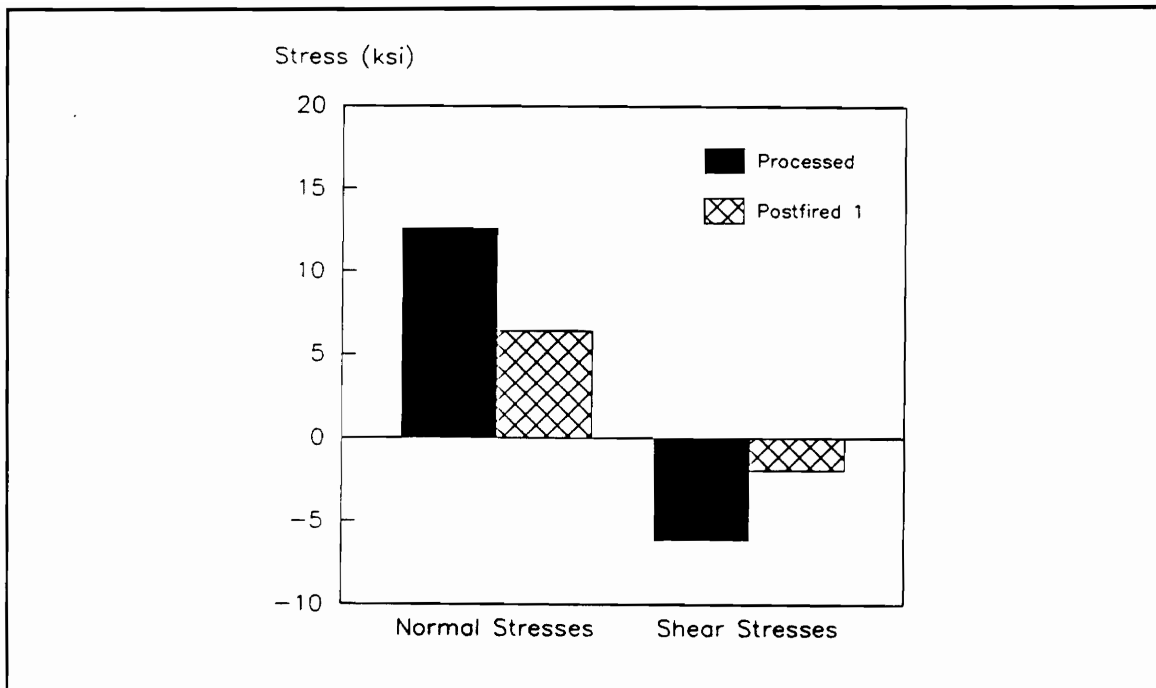

Figure 6.4: Comparison of Normal and Shear Stresses for High Temperature Anneal.

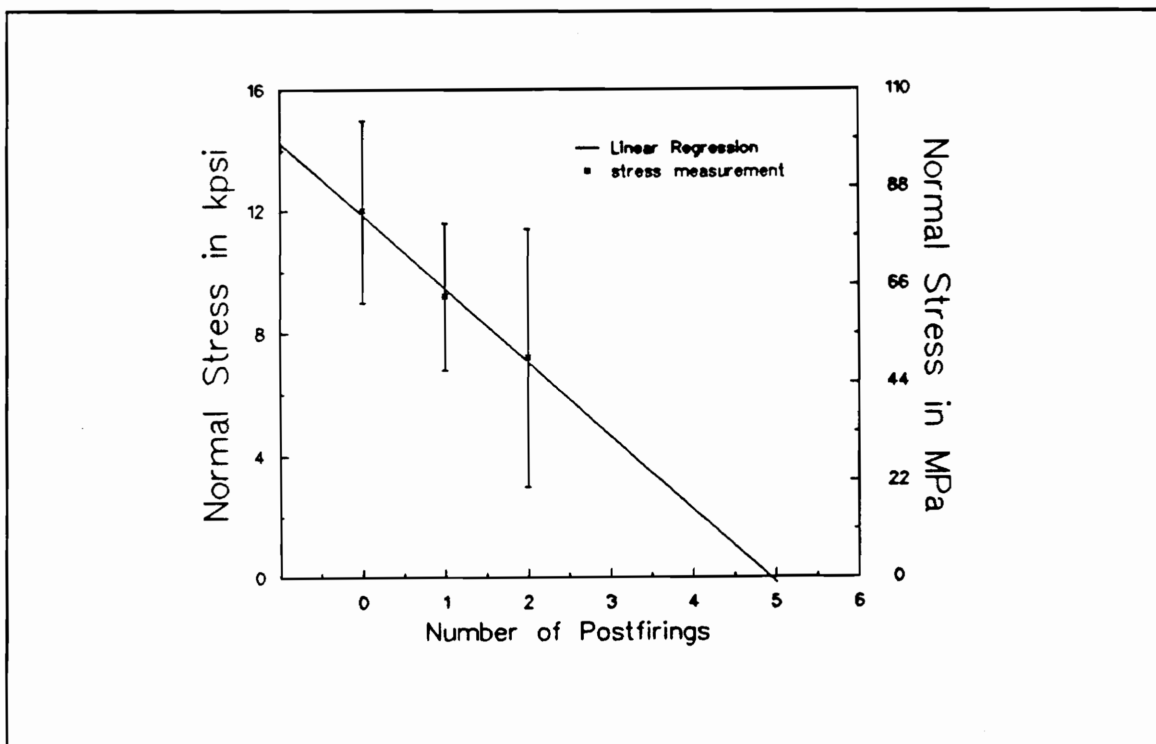

Figure 6.5: Linear Regression of Low Temperature Anneal Stresses

production level, device fabrication procedures would have to be altered. Substrates would be cut to size, annealed, and then processed. While this order may relieve stresses, the odd shapes of the substrate may make printing more difficult. In addition, this annealing step requires a special high temperature furnace.

It is crucial that these two annealing steps be studied further to determine how stresses may be economically and efficiently relieved. Such stress reduction should decrease failures due to fracture and improve production yield as well as improve the uniformity and performance of electrical characteristics.

6.3 Residual Stresses in the Metallization

The electrical properties of thick film structures are determined by the interaction of the substrate and paste. As discussed in the previous section, the investigations have clearly found that stresses are induced in the substrate by processing. The thickness of the substrate investigated was 635 microns (25 mils). However, the maximum thickness of the metallization was approximately 25 microns (1 mil). Because of the small thickness of the metallization, if there is good adhesion between the metallization and the substrate one would expect that the stress gradient would be more pronounced in the metallization as compared to the substrate material. Combining the stress information related to the substrate and metallization might explain the interaction between stresses and electrical characteristics observed in the circuit.

Using the procedures described in Chapter 5, the residual stresses in the metallization were investigated. The (222) planes of the Ag-Pd metallization produced excellent diffraction peaks at a variety of psi angles. The integrated intensity of the diffraction peak as a function of ψ was constant, indicating no preferred orientation in the metal. As indicated in Chapter 5, no experimental values for the x-ray elastic constant were available for the Ag-Pd metallization. Using materials properties from Simmons and Wang [37] and following the procedures of Noyan and Cohen [21], we have estimated the constant $(E/(1+\nu))$

for the bulk alloy to be $8.55 * 10^6$ psi ($58.9 * 10^9$ Pa). We believe this value to be accurate within 10 to 20 %.

Results from measurements on metallization on two probes are shown in Table 6.4. These results show that the stresses in the fired metallization are tensile and very large, averaging about 7.7 ksi (53 MPa). The calculation of such stresses is based on our assumption that the metallization behaves mechanically the same as bulk alloy. If such is not the case, the estimate of the x-ray elastic constant described in the previous paragraph is invalid.

Qualitatively, it is easy to understand why the stresses in the metallization are tensile. Since the coefficient of linear thermal expansion of alumina (Al_2O_3) is roughly a factor of three smaller than that of Ag (and therefore presumably of Ag-Pd alloys) and since the bonding between the metallization and the substrate occurs at the high firing temperature, the metallization is expected to shrink faster than the ceramic upon cooling. Thus, the substrate in contact with the metal will be in compression and the metal will be in tension. This explanation is in complete agreement with our observations reported in Section 6.2.2 that the back side of the substrates is also in tension as shown in Figure 6.6. Thus, by combining stress measurements from both materials in this two material system we can confirm the theoretical interactions caused by differences in TCE.

Although the stresses in the metallization are smaller than those in the alumina substrate, the TDR experiments in the next section indicate a relationship between processing induced stresses and variation in electrical performance of the probe. These results show that the electrical characteristics of the metallization are extremely sensitive to even small stresses in the material.

Several points must be kept in mind when interpreting these data. First, the actual stresses in the metallization may differ significantly from our estimates if the metallurgical microstructure of the fired metallization differs significantly from that of the bulk material for which we were able to find elastic constants. Second, although there appears to be a significant effect of these stresses on the TDR waveforms as will be shown in the next section, as long as these stresses are constant in time, it is not yet clear whether they have

Table 6.4: Normal Stresses in Ag-Pd Metallization

Substrate	Normal Stresses ksi	(MPa)
Sample 1		
Meas. 1	7.4 ±2.0	(51.0±13.8)
Meas. 2	7.5±2.6	(51.7 ±17.9)
Meas. 3	6.4±3.0	(44.1 ±20.7)
Sample 4		
Meas. 1	8.1± 2.8	(55.8±19.0)
Meas. 2	8.7± 2.4	(60.0 ±16.5)
Meas. 3	8.3±1.8	(57.2±12.4)

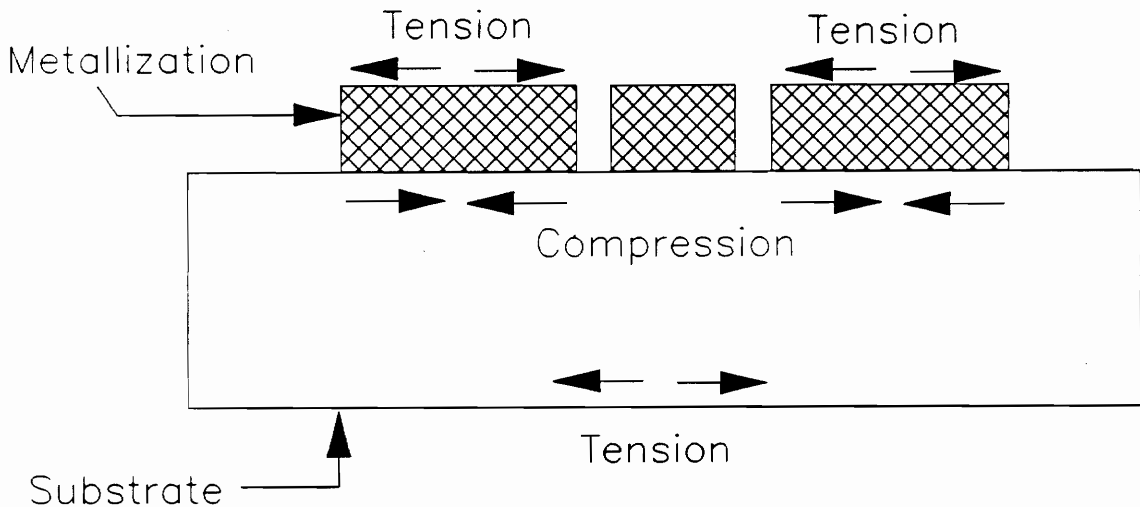

Figure 6.6: Stresses in Circuit Due to TCE Mismatch.

any significant detrimental effect on the performance of the probe.

6.4 Time Domain Reflectometry Measurements

Graphs used to compare before trimming and after trimming results on all eight probes clearly show that laser trimming changes the characteristics of the probe. While some probes only changed slightly, several other probes differed substantially from the original waveform. Two examples of these variations are shown in Figure 6.7.

These figures represent the TDR response of the connector, the solder connection, and the probe. The time from 0 to 37.5 ns represents the coaxial cable as seen earlier in Figure 5.7. The variation in the waveform around 37.5 ns is due to the solder joint. Since the probe was disconnected from the MELJ connector before laser trimming and then reconnected, the characteristics of the solder joint is expected also to change slightly. This can be verified by resoldering the same probe and measuring several times. In addition to this effect, the graphs show changes over the entire probe as seen in these figures.

Since the only changes in these probes are those caused by laser scribing, it seems reasonable to assume a cause and effect relationship between the processing and the changes in electrical properties of the probe. As discussed in the above section, laser trimming was also found to induce residual stresses in the substrate. These two results lead to the conclusion that the changes in residual stresses in the substrate and/or metallization are responsible for the changes in the electrical characteristics. This conclusion is supported by previous work where thick film resistors are used as strain gauges.

Because of time constraints and the complexity of the model for the coplanar probe, modeling of the TDR traces was not completed in time for inclusion into this thesis. This work is relevant and will be incorporated into a future publication.

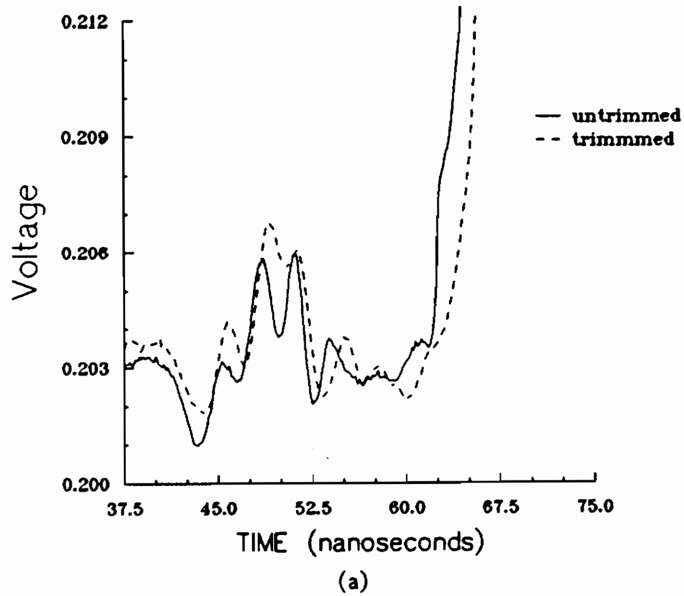

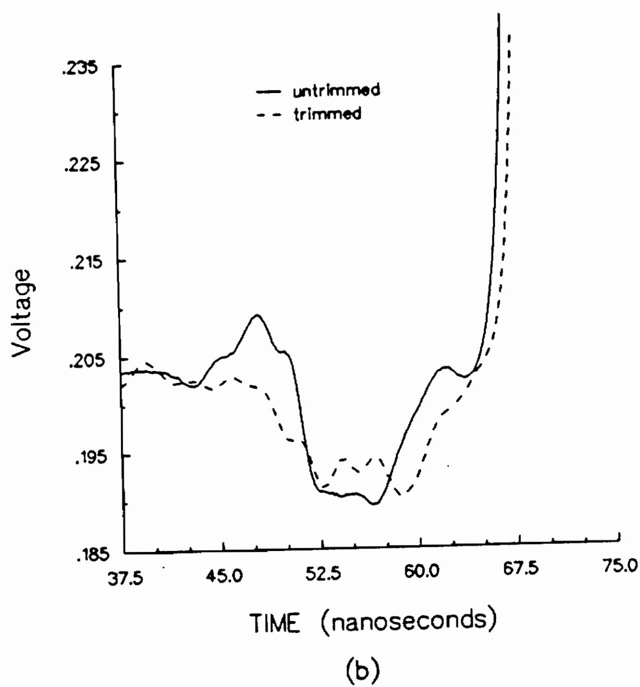

Figure 6.7: Comparison of TDR Open Circuit Measurements before and after laser cutting: (a) Probe T10 (b) Probe T9.

6.5 Summary

This chapter has reported the results and interpretation of experiments performed on the coplanar probe. This work included the combination of x-ray diffraction techniques for measuring residual stresses as a function of processing parameters and annealing, and time domain reflectometry to determine electrical performance as a function of processing parameters.

Chapter 7

CONCLUSIONS AND SUGGESTED FUTURE WORK

Although this work represents exploratory research, several important conclusions may be drawn. These conclusions can be divided into two major categories: conclusions concerning stresses in thick film circuits and conclusions concerning TDR measurements. Each will be discussed here. Finally this chapter also presents recommendations for future work.

Conclusions concerning the residual stresses in the coplanar probe may be divided into four categories: stresses in the bare substrate, stresses induced by processing, stresses reduced by annealing, and stresses developed in the metallization.

The bare substrates, as received from the vendor, show two major features. First, the substrates are essentially stress-free both parallel and perpendicular to the substrate edges. A small shear stress represents the rotation of the stress ellipsoid from the axes of measurement. Second, the substrate is homogeneous stress-wise across the sample. No statistical difference was found between the center, the edges, and the corners. This finding is significant because stress measurements can be made at one spot on the substrate and these values represent the stresses in that substrate. Another important conclusion is that using proper statistical design of the measurements and repetitions of the experimental

measurement, one can reduce the errors caused by misalignment of the sample.

While understanding the stresses in the substrate was the basis for other work, the bulk of important measurements dealt with the role of processing on stresses in the ceramic substrate. Our research showed that the printing and firing steps of thick film manufacture cause small tensile stresses in the back of the substrate. These stresses are attributed to the mismatch of the thermal coefficients of linear expansion between the substrate and the deposited metallization. In addition, laser trimming induced large stresses, as much as forty percent of the fracture strength of the substrate. These stresses have lead to a lower yield of parts and premature fracture of parts during testing or packaging. The stresses induced by the processing steps of printing/firing and laser cutting are significant and cannot be dismissed.

The two annealing experiments provided information on how these stresses can be reduced to help prevent fracture of the part. The production temperature anneal provided a stress reducing technique which does not require extra equipment. However, stresses were reduced slowly so repeated firings were necessary. Also, the shear stresses in this process were not reduced. The secondary high temperature anneal provided an alternative in which the normal and shear stresses were both reduced. However, the optimal peak temperature and cooling rate remain to be determined. In addition, this method involves the additional expense of a high temperature furnace. Finally, the high temperature anneal requires modification of the manufacture procedure because it is much above the melting point of the metallization.

The stresses in the metallization hold the key to understanding how the electrical properties of the circuits are affected by stress. The stress values measured in the metallization coupled with the stresses in the ceramic indicate that the manufacturing process causes changes in the materials properties that affect the electrical performance of the circuit. While only small tensile stresses were found in the metallization, the electrical properties seem to be very stress sensitive.

The TDR measurements are the tool used to determine the changes in the electrical

properties of the probe. While qualitatively these changes can be observed by differences in the voltage traces, the real value of this method is the ability to model the trace and determine its corresponding electrical model. This and other information can be determined by further study in this area.

This work represents the exploratory efforts to determine what stresses can be measured and whether the electrical properties are affected by these stresses. The results of this work have opened several new possibilities for continued research. The first area needing more work is the study of stresses in the metallization. This can be accomplished by using various microscopy techniques to determine the interaction between the substrate and metallization.

Second, an experimental correlation between the residual stresses in the ceramic substrate and in the metallization with the TDR measurements must be determined. This can be accomplished by taking a large sample of probes from bare substrate to finished trimmed probes and measuring the residual stresses in the substrate and in the metallization as well as taking TDR measurements at various processing stages. Then processing parameters can be varied to determine their effect on electrical performance by doing extensive modeling of the TDR traces.

Third, a significant research effort needs to be mounted to determine the optimal conditions for relieving the stresses in both the substrate and in the metallization. Clearly, stress reduction in the substrate will reduce failures due to fracture and improve product yield, while elimination of stresses in the metallization should improve the uniformity and performance of the TDR response.

The fourth and final step is to apply the knowledge gained from the simple probe circuit to more complicated thick film circuits. This can be achieved by repeating the stress characterization and the electrical testing on these circuits to understand the role of stresses in their electrical performance.

Appendix A

Calculations

A.1 Calculation of Stresses

Equation 3.3 shows the relationship between d-spacing and stresses.

$$\frac{d_{0,\psi} - d_{0,0}}{d_0} = \frac{1+\nu}{E}\left[\sigma_{11}\sin^2\psi + \sigma_{13}\sin 2\psi\right]$$

Calculations of the stresses in a sample can be determined by the following procedures:

Regression versus $sin^2\psi$

When the sample contains only normal stresses, σ_{13} is zero. Rearranging the above equation gives:

$$d_{0,\psi} = \frac{1+\nu}{E}\, d_0\ \sigma_{11}\ sin^2\psi + d_{0,0}$$

where the slope and intercept of a regression of d versus $sin^2\psi$ are shown below:

$$slope = \frac{1+\nu}{E}\, d_0\ \sigma_{11}$$

$$intercept = d_{0,0}$$

Using the slope, the normal stress value σ_{11} can be determined. The value $d_{0,0}$ is substituted for d_0.

$$\sigma_{11} = \frac{\text{slope } E}{d_{0,0}\ (1+\nu)}$$

Multiple Regression versus $sin^2\psi$ and $sin2\psi$

If shear stresses are present, a multiple regression is necessary. This regression is also done on a modified version of equation 3.3.

$$d_{0,\psi} = \frac{1+\nu}{E}\ d_0\ (\sigma_{11}\ sin^2\psi + \sigma_{13}\ sin2\psi) + d_{0,0}$$

The multiple regression results in two coefficients as well as an intercept. These equation are given by:

$$\begin{aligned}
\text{coefficient of } sin^2\psi &= \frac{1+\nu}{E}\ d_0\ \sigma_{11}\ = m_1 \\
\text{coefficient of } sin2\psi &= \frac{1+\nu}{E}\ d_0\ \sigma_{13}\ = m_2 \\
\text{intercept of regression} &= d_{0,0}
\end{aligned}$$

To determine the normal and shear stresses, the above coefficients were solved for σ_{11} and σ_{13} respectively. As with the above method, $d_{0,0}$ was substituted for d_0.

$$\begin{aligned}
\sigma_{11} &= \frac{E}{(1+\nu)\ d_{0,0}}\ m_1 \\
\sigma_{13} &= \frac{E}{(1+\nu)\ d_{0,0}}\ m_2
\end{aligned}$$

A.2 Calculation of Diffracted Planes in Ag-Pd

From experiments: $2\theta = 156^o$ so $\theta = 78^o$.

Using equation 3.1, the d-spacing corresponding to this angle can be determined.

$$n(\lambda) = 2d \sin\theta$$

For Cr Kα radiation, $\lambda = 2.290\mathring{A}$.

$$d_{hkl} = \frac{n\lambda}{2sin\theta} = n\ 1.17058\mathring{A}.$$

$$n = 1 \quad d_{hkl} = 1.1706\ \mathring{A}.$$

$$n = 2 \quad d_{hkl} = 2.3412\ \mathring{A}.$$

$$n = 3 \quad d_{hkl} = 3.5117\ \mathring{A}.$$

From [39], a d-spacing of 1.1796 Å was reported for the (222) planes of silver. The calculated experimental value is smaller than this value because of the influence of the palladium on the alloy.

Bibliography

[1] Baker, E., "Some Effects of Temperature on Material Properties and Device Reliability", IEEE Transactions on Parts, Hybrids, and Packaging, Vol. PHP-8, No. 4, Dec. 1972, pp. 4-14.

[2] Yasukawa, A. and T. Sakamoto, "Stress Analysis and Hybrid Technology", The International Journal for Hybrid Microelectronics, Vol. 11, No. 1, 1988, pp. 12-16.

[3] Riemer, D.E., "The Effect of Thick-Film Materials on Substrate Breakage During Processing", The International Journal for Hybrid Microelectronics, Vol. 6, No. 1, Oct. 1983, pp. 599-602.

[4] Shah, J.S. and L. Berrin, "Mechanism and Control of Post-Trim Drift of Laser-Trimmed Thick-Film Resistors", IEEE Transactions on Components, Hybrids, and Manufacturing Technology, Vol. CHMT-1, No. 2, June 1978, pp. 130-136.

[5] Riemer, D.E. and J.D. Russell, "The Optimized Solder Bond For Ceramic Chip Carriers on Ceramic Boards", The International Journal for Hybrid Microelectronics, Vol. 6, No. 1, Oct. 1983, pp. 217-222.

[6] Reshey, J., "Thick-Film Thermal Stress Induced by Lid-Seal Epoxy", Proceedings of the 1985 International Symposium on Microelectronics, ISHM, Reston, Virginia, 1985, pp. 513-519.

[7] Holmes, P.J., "Changes in Thick-Film Resistor Values Due to Substrate Flexure", Microelectronics and Reliability, Vol. 12, 1973, pp. 395-396.

[8] Morten, B., L. Pirozzi, M. Prudenziati, and A. Taroni, "Strain sensitivity in film and cermet resistors: measured and physical quantities", Journal of Physics D: Applied Physics, Vol. 12, 1979, pp. L51-L54.

[9] Canali, C., D. Malavasi, B. Morten, M. Prudenziati, and A. Taroni "Piezoresistive effects in thick-film resistors", Journal of Applied Physics, Vol. 51, No. 6, June 1980, pp. 3282-3288.

[10] Canali, C., D. Malavasi, B. Morten, M. Prudenziati, and A. Taroni "Strain Sensitivity in Thick-Film Resistors", IEEE Transactions on Components, Hybrids, and Manufacturing Technology, Vol. CHMT-3, No. 3, Sept. 1980, pp. 421-423.

[11] Shah, J.S., "Strain Sensitivity of Thick-Film Resistors", IEEE Transactions on Components, Hybrids, and Manufacturing Technology, Vol. CHMT-3, No. 4, Dec. 1980, pp. 554-564.

[12] Dell'Acqua, R., G. Dell'Orto, A. Simonetta, and C. Canali, "Long Term Stability of Thick Film Resistors Under Strain", The International Journal for Hybrid Microelectronics, Vol. 5, No. 2, 1982, pp. 82-85.

[13] Nielsen Jr., H.A., "The Thick-Film Strain Gage", Experimental Techniques, Vol. 12, No. 1, Jan. 1988, pp. 19-22.

[14] Cattaneo, A., R. Dell'Acqua, G. Dell'Orto, L. Pirozzi, and C. Canali, "A Practical Utilization of the Piezoresistive effect in Thick Film Resistors: A Low Cost Pressure Sensor", Proceedings of the 1980 International Symposium on Microelectronics, ISHM, Reston, Virginia, 1980, pp. 221-228.

[15] Dell'Acqua, R., G. Dell'Orto, F. Forlani, A. Puzonni, and C. Canali, "Characteristics and Performances of Thick Film Pressure Sensors for Automotive Applications", Sensors and Actuators, Feb. 1982, pp. 69-75.

[16] Glas, H.J., W. Kuhnt, and G. Stecher, "Integrated Hybrid Pressure Sensor Using a Piezoresistive Thick-film Sensor Element", Sensors and Actuator 1987, Feb. 1987, pp. 1-6.

[17] Muthukrishnan, N., S.M. Riad, and A. Elshabini-Riad, "A Thick-Film Coplanar Probe for Time Domain Measurements", IEEE Transactions on Components, Hybrids, and Manufacturing Technology, Vol. CHMT-12, No. 2, 1989, pp. 297-302.

[18] Mura, T., Micromechanics of Defects in Solids, Martinus Nijhoff Publishers, The Hague, Netherlands, 1982.

[19] Sabol, S.M. and J.A. Sullivan III, "Mechanically Induced Residual Stress in Al_2O_3-20%ZrO_2 and correlations with Microhardness", Senior thesis, Dept. of Materials Engineering, VPI&SU, May 1988.

[20] Middleton, J.C., "Residual Stresses and X-rays", NDT International, Vol. 20, No. 5, Oct. 87, pp. 291-294.

[21] Noyan, I.C. and J.B. Cohen, Residual Stress: Measurement by Diffraction and Interpretation, Springer-Verlag, New York, 1987.

[22] Tanaka, K., Y. Yamamoto, and K. Suzuki, "Elastic Constants of Ceramics for X-ray Residual Stress Measurements", International Conference on Residual Stresses, edited by G. Beck, S. Denis, and A. Simon, Elsevier Applied Science, New York, 1989, pp. 328-334.

[23] Hauk, V., "Residual Stresses, Their Importance in Science and Technology", Residual Stresses, edited by E. Macherauch and V. Hauk, Proceedings of the European Conference on Residual Stresses 1983, Karlsruhe, Informationsgesellschaft Verlag, Oberursal, West Germany, 1984, pp. 9-45.

[24] Eigenmann, B., B. Scholtes, and E. Macherauch, "X-Ray Stress Determination in Ceramic and Ceramic-Metal Composites", International Conference on Residual Stresses, edited by G. Beck, S. Denis, and A. Simon, Elsevier Applied Science, New York, 1989, pp. 27-38.

[25] Ruud, C.O., C.P. Gazzara, D.J. Snoha, D.P. Ivkovich, and D.P. Hasselman, "X-ray Stress Measurement of Structural Ceramics", Materials Characterization

For Systems Performance and Reliability, edited by James W. McCauley and Volker Weiss, Plenum Publishing Corporation, 1986, pp. 361-383.

[26] Lange, F.F., M.R. James, and D.J. Green, "Determination of Residual Surface Stresses Caused by Grinding in Polycrystalline Al_2O_3", Journal of the American Ceramics Society, Vol. 66, No. 2, Feb. 1983, pp. C16-C17.

[27] Tanaka, K., K. Suzuki, and Y. Yamamoto, "Residual Stress Effect on Fracture Strength of Ceramics", International Conference on Residual Stresses, edited by G. Beck, S. Denis, and A. Simon, Elsevier Applied Science, New York, 1989, pp. 15-26.

[28] Ruud, C.O. and C.P. Gazzara, "Residual Stress Measurements in Alumina and Silicon Carbide", Journal of the American Ceramic Society, Vol. 68, No. 2, Feb. 1985, pp. C67-68.

[29] Gardner, T.J., and E.K. Beauchamp, "The Effect of Laser Machining on the Strength of Al_2O_3 Substrate Materials", International Symposium on Machining of Advanced Ceramics Materials and Components, Apr. 1987, pp. 249-255.

[30] Nahman, N.S., unpublished work.

[31] Elshabini-Riad, A. and N. N. Schulz, "Electrical Modeling", ISHM Modules, Chapter 16, ISHM, Reston, Virginia, in press.

[32] Toscano, J.C., "Wideband Characterization of Thick Film Inductors", Master's Thesis, VPI&SU, March 1988.

[33] Kyocera Data Sheet, Kyocera Properties for Substrate and Lid Materials, Somerset, NJ 08873.

[34] Private Communication, S. Gordon, DuPont Electronics, Barley Mill Plaza, P.O. Box 80030, Wilmington, Delaware, 19880.

[35] Foster, D.C. and R.E. Tontodonato, "Correlation of X-ray Determined Residual Stress with Rupture Modulus in Al_2O_3", senior thesis, Dept. of Materials Engineering, VPI&SU, May, 1988.

[36] ABstat^{TM}, AndersonBell, 11479 S. Pine Dr., Parker, CO 80134.

[37] Simmons, G. and H. Wang, Single Crystal Elastic Constants and Calculated Aggregate Properties: A Handbook, second edition, M.I.T. Press, Cambridge, Massachusetts, 1971.

[38] Barrett, C.R., W.D. Nix, and A.S. Tetelman, The Principles of Engineering Materials, Prentice-Hall, Inc., Englewood Cliffs, 1973.

[39] Powder Diffraction File for Silver, International Centre for Diffraction Data, Swarthmore, PA, 1986.

VITA

Ms. Noel Nunnally Schulz was born in Charlottesville, Virginia on July 14, 1966. She received her B.S. in Electrical Engineering from Virginia Polytechnic Institute and State University (VPI&SU) in May 1988. Her professional work experience includes two summers working in Detroit, Michigan for General Motors CPC Engineering Laboratories, and two summers working as an engineer for Poly-Scientific in Blacksburg, Virginia.

Since August 1988, she has worked as a Graduate Teaching Assistant and Graduate Research Assistant in the Electrical Engineering Department at VPI&SU. In February 1990, she completed the requirements for a M.S. in that department.

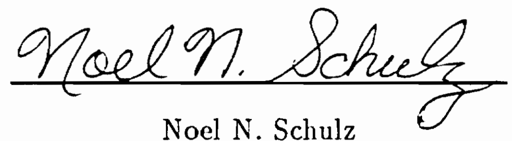

Noel N. Schulz